Lund University

Master's Thesis

Tagging of Boosted Top Quarks using Reclustered Jets

Author:
Jakob Calvén

Supervisor:
Prof. Torsten Åkesson

A thesis submitted in fulfilment of the requirements for the degree of Master of Science

in the

Div. of Particle Physics
Department of Physics

September 2014

LUND UNIVERSITY

Abstract

Faculty of Science
Department of Physics

Master of Science

Tagging of Boosted Top Quarks using Reclustered Jets

by Jakob Calvén

The ability to identify boosted top quarks will be of great importance in searches for new physics at the LHC, as boosted tops play an important role in many scenarios of physics beyond the Standard Model. One top tagging algorithm that has been successfully used in the ATLAS collaboration is the HEPTopTagger, which exploits the clustering history of Cambridge/Aachen (C/A) jets to filter out everything but the core objects inside the jets in an attempt to identify those originating from top quark decay. However, as most physics studies in ATLAS uses another jet algorithm, the anti-k_t algorithm, it is of interest to know whether top tagging with the HEPTopTagger is possible on jets initially clustered with anti-k_t . This thesis presents such a study, and it is found that the HEPTopTagger can be used with equal performance on anti-k_t jets as C/A jets. Furthermore, it is demonstrated that the HEPTopTagger with anti-k_t jets provide an exciting possibility for the discovery of heavy resonances decaying to boosted top-antitop quarks in dijet mass searches. In particular, we consider the top-antitop decay of a Kaluza-Klein gluon with a mass of 3 TeV.

Populärvetenskaplig sammanfattning

Standardmodellen, vår nuvarande fysikaliska modell för att beskriva fundamentalpartiklar och deras växelverkan, har mött en enorm framgång genom åren – samtliga partiklar och växelverkningar som standardmodellen beskriver har bekräftats experimentellt. Standardmodellen har dock problem med att förklara vissa egenskaper hos partiklarna,och den är inte förenlig med gravitationskraften; en av de fyra fundamentala krafterna i naturen. Detta gör att standardmodellen av många anses vara en manifestation av en mer fundamental teori, giltig vid låga energier.

Vid partikelfysiklaboratoriet CERN utanför Geneve, kollideras protoner i partikelacceleratorn Large Hadron Collider (LHC) – världens största och mest kraftfulla partikelacceleratoranläggning – i hopp om att ge ny insikt om naturens allra minsta beståndsdelar. I kollisionerna omvandlas partiklarnas rörelse- och massenergi till nya partiklar. Dessa partiklar är inte jämnt fördelade över alla vinklar utan har en tendens att klumpa ihop sig inom mindre områden, i så kallade jettar.

Den här uppsatsen behandlar frågan om den algoritm som vanligtvis används för att rekonstruera jettar i ATLAS-experimentet vid LHC, den så kallade anti-k_t-algoritmen, är kompatibel med en särskild metod för att identifiera energetiska toppkvarkar, känd som "HEPTopTagger". Att identifiera energetiska toppkvarkar är särskilt intressant då många lovande utvidgningar av standardmodellen förutsäger nya, tunga, partiklar som framförallt sönderfaller till toppkvarkar med hög kinetisk energi. Av den anledningen anses toppkvarken utgöra en av de viktigaste signalerna för ny fysik.

Toppkvarken sönderfaller främst till en bottenkvark, samt en kvark och en antikvark via utsöndringen av en W-boson (en av kraftförmedlarna av den svaga kraften), i vad som kallas för det hadroniska toppsönderfallet. När toppkvarken produceras vid låga energier, är dess sönderfall separerat i tre distinkta jettar och tekniker för att identifiera sådana toppkvarkar är väl utvecklade. Om, däremot, toppkvarken har en hög energi, till exempel om den producerats i sönderfallet av en tung, ny, partikel, tenderar de tre distinkta jettarna från sönderfallet att närma sig varandra till den grad att de inte längre går att urskilja individuellt. Istället för att försöka identifiera tre distinkta jettar som är det typiska signalementet för ett hadroniskt toppkvarkssönderfall, utnyttjar HEPTopTagger istället idén att hela sönderfallet klumpas ihop i en stor jet. Genom analys av den inre strukturen i en sådan jet, så kallad sub-strukturanalys, kan metoden identifiera om jetten härrör från ett toppkvarksönderfall.

HEPTopTagger har typiskt använts på jettar som konstruerats med en algoritm annan än anti-k_t, då anti-k_t-jettar saknar den information som är nödvändig för substrukturanalys. I det här arbetet undersöks möjligheten att först konstruera jettar med anti-k_t-algoritmen, sedan omrekonstruera dem med en algoritm som är bättre lämpad för subtrukturanalys, för att slutligen försöka identifiera toppkvarkar med hjälp av HEPTopTagger. Ett sådant förfarande är av intresse att undersökas, bland annat då tidigare jetanalyser i ATLAS kan återanvändas för att leta efter toppkvarkar med HEPTopTagger. Det här arbetet visar att HEPTopTaggers förmåga att korrekt identifiera toppkvarkar inte försämras vid ett sådant förfarande.

Tidigare analyser med HEPTopTagger har indikerat att metoden fungerar väl till att identifiera måttligt energetiska toppkvarkar. Det här arbetet visar att HEPTopTagger även går att använda vid mycket engergetiska toppkvarksönderfall, vilket demonstreras i en exempelanalys, i vilket en ny, tung, partikel som sönderfaller till ett toppkvark-antitoppkvark-par, identifieras med hög signifikans med hjälp av HEPTopTagger.

Acknowledgements

I would like to thank my supervisor, Torsten Åkesson, for introducing this project to me and for continuously contributing new ideas to the analysis. Much gratitude is directed towards Lene Bryngemark, without whom this project would not have been possible, for always being present in the weekly (and at one point, daily) meetings, and for tirelessly sharing her expertise on the subject. Most of all, I want to thank my loving wife for her enormous patience throughout this endeavor, and for always keeping my spirit to move forward high. For this, I am forever in debt.

Contents

Chapter 1

Introduction

The motivation for scientific endeavors is often not only to gain knowledge, but also understanding. The Standard Model of particle physics is one of the greatest achievements in physics, allowing physicists to achieve astonishing advances in the understanding of nature's most fundamental workings. Ever since it was developed in the early 1970's, The Standard Model has allowed for remarkably accurate predictions, one after the other confirmed by experimental results. However, the Standard Model does not tell us everything. For instance, neutrino mixing or dark matter, both of which have been established experimentally or by observations, can not be explained by the Standard Model. For this reason, it is believed that the Standard Model is not the whole story, but instead a low-energy manifestation of a much more encompassing theory. The quest for new physics, that could indicate whether this notion carries any merit, is one of the objectives of the Large Hadron Collider at CERN which is exploring new territories in the energy-regime.

This thesis is outlined as follows: In the second chapter, a short presentation of the Standard Model is provided, along with an introduction to a particular extension of the Standard Model that requires one extra dimension of space. The third chapter provides a short description of the Large Hadron Collider (LHC) and the ATLAS experiment. In the fourth chapter, so-called jet algorithms are described, as well as a special kind of algorithm designed to identify top quarks, which is essential for this thesis. The fifth chapter contains an analysis of two top tagging procedures, with the aim of providing new information about the usage of a particular jet algorithm. In the sixth, and last chapter, the results from chapter four are put to test in a dijet mass analysis of a particular heavy resonance that is predicted by the extra-dimensional extension to the Standard Model discussed in chapter two.

Chapter 2

Theory

2.1 The Standard Model of Particle Physics

The Standard Model (SM) is a theory that describes all known elementary particles and their interactions by combining the theories of electroweak interactions and Quantum Chromodynamics (QCD). Some important results of the Standard Model, and extensions to it, are presented in this chapter to give the reader a sense of the physics of interest for this thesis.

The particles in the Standard Model are subdivided into two main classes based on their spin: fermions, which all have half-integer spins, and bosons, which all have integer spin values. Although most particles are compositions of other particles, there are a few particles that, as far as we know, do not have an internal structure. These elementary particles are classified as quarks, leptons, gauge bosons and the Higgs boson. Quarks and leptons belong to the group of fermions and have spin-$\frac{1}{2}$, gauge bosons belong to the group of bosons and have spin-1, while the Higgs boson, also belonging to the boson group, has spin-0.

The quarks and leptons come in doublets and are grouped into three generations, mainly distinguished by their masses. Each generation consists of a charged lepton, a neutral neutrino and an up-type and down-type quark. Table 2.1 summarizes the fermions. While quarks are subject not only to the strong force (*i.e.* QCD) but also the weak and electromagnetic force, only the weak force is acting on *all* leptons. As opposed to the neutrinos, which do not carry an electric charge, the charged electron, muon and tau are additionally subject to the electromagnetic force. Associated to every fermion is an anti-particle which has the same quantum numbers but opposite charge. Neutrinos and

antineutrinos, which do not carry any charge, differ only in chirality, or handedness[1]. So far, only left-handed neutrinos and right-handed antineutrinos have been observed.

TABLE 2.1: Table of fermions sorted by generation.

	I	II	III
Quarks	up down	charm strange	top bottom
Leptons	ν_e e^-	ν_μ μ^-	ν_τ τ^-

Mathematically, the Standard Model is a local non-abelian gauge field theory based on the symmetry group $SU(3)_C \times SU(2)_L \times U(1)_Y$, where $SU(3)_C$ is the symmetry group of the strong interaction of QCD, and $SU(2)_L$ together with $U(1)_Y$ are the symmetry groups describing the electroweak interaction. The symmetry group of the SM imposes a symmetry on the SM Lagrangian, notably that it is invariant under space-time dependent continuous internal transformations of the group. This is referred to as gauge invariance. Any quantum field in the SM is required to ensure gauge invariance. The fourth fundamental force, gravity, is not described by the Standard Model, and its effect can usually be ignored in the context of particle physics due to its comparably tiny interaction strength (10^{25} times smaller than the weak interaction). However, the effect of gravity does become important in some scenarios beyond the SM, as will be discussed in Section 2.2.

2.1.1 The strong interaction

The strong interaction (the interaction of particles that carry color charge; the quarks and the gluons) is described by Quantum Chromodynamics. The color charge comes in three different types, conventionally denoted as red (r), blue (b) and green (g). Corresponding to each color is an anticolor ($\bar{r}, \bar{b}, \bar{g}$), carried by antiquarks.

In QCD, quarks form color triplets and interact with an octet of gluons carrying two color charges. The QCD Lagrangian can be written as:

$$\mathcal{L}_{\text{QCD}} = \bar{\psi}_i(i\gamma^\mu\partial_\mu - m_i)\psi_i - gG^a_\mu\bar{\psi}_i\gamma^\mu T^a_{ij}\psi_j - \frac{1}{4}G^a_{\mu\nu}G^{\mu\nu}_a, \tag{2.1}$$

where i is the index of the quark flavor and a the color state of the gluon. The quark masses are denoted by m_i and the strong coupling constant by g. $\psi_i(x)$ is the quark field and $G^a_\mu(x)$ are the gluon fields. The gluon field tensor is:

$$G^a_{\mu\nu} = \partial_\mu G^a_\nu - \partial_\nu G^a_\mu - gf^{abc}G^b_\mu G^c_\nu, \tag{2.2}$$

[1]Handedness refers to the direction of a particle's spin. A particle is called right-handed if its spin is in the same direction of its motion, and left-handed if its spin is in the opposite direction of its motion.

where f^{abc} are structure constants defined by the commutation relations of the group tensors T^a_{ij}. Included in the Lagrangian are kinetic terms of the quark and gluon fields, the color interaction and gluon self coupling.

Due to a phenomena known as *color confinement*, quarks and gluons can only exist as color-neutral combinations, called *hadrons*. After a high-energy collision in a hadronic particle accelerator, the hadronic state of recoiling partons (quarks or gluons) will break apart as they move away from each other; a process called *fragmentation*. The reason for the fragmentation is that it becomes energetically favorable to create a quark-antiquark pair from the vacuum with which the partons can form new color-neutral states, rather than keeping the original hadron together. The fragmentation process produces a shower of quarks and gluons which recombine as hadrons. This process is called hadronization, and because of momentum conservation, the products from the hadronization appear as sprays of particles moving in the similar direction as the original parton, in what is called a *jet*.

2.1.2 The electroweak interaction

The electromagnetic and weak interactions are unified into the electroweak interaction by the $SU(2)_L \times U(1)_Y$ gauge group. $SU(2)_L$ introduces three gauge fields W^a_μ, while $U(1)_Y$ introduces the gauge field B_μ. The physical $W^\pm$ bosons, neutral vector boson Z^0 and the electromagnetic field (photon) A correspond to linear combinations of W^a_μ and B_μ:

$$W^\pm_\mu = \frac{1}{\sqrt{2}}(W^1_\mu \mp iW^2_\mu) \tag{2.3}$$

$$Z_\mu = W^3_\mu \cos\theta_W - B_\mu \sin\theta_W \tag{2.4}$$

$$A_\mu = W^3_\mu \sin\theta_W + B_\mu \cos\theta_W, \tag{2.5}$$

where θ_W is the weak mixing angle. The symmetry group of the electroweak interaction is a subset of the SM symmetry group, and must also preserve gauge invariance. Because of this, the gauge bosons need to enter as massless particles in the electroweak theory, as adding mass terms to the gauge fields breaks the gauge invariance. Since the gauge bosons associated with the weak interaction have a rather large mass (unlike the massless photons and gluons), there is seemingly a contradiction between the theoretical prediction and the experimental observation.

2.1.3 The Higgs mechanism

To allow for the weak gauge bosons, the W and Z, to be massive, it is required that the electroweak symmetry is spontaneously broken[2]. Otherwise, all bosons would be massless. The Higgs mechanism is a solution to this problem. It introduces a field with a nonzero vacuum expectation value which breaks the symmetry property of the vacuum state. The Higgs field, ϕ, is a complex doublet (*i.e.* it has two complex components) of the $SU(2)$ group:

$$\phi = \begin{pmatrix} \phi^+ \\ \phi^0 \end{pmatrix}, \tag{2.6}$$

where ϕ^+ and ϕ^0 are the two components of the Higgs field, and the superscripts $^+$ and ^{0} indicate the electric charge of the components. To ensure that the vacuum is electrically neutral, only the neutral component of the Higgs field is assigned a real nonzero vacuum expectation value, v:

$$\langle 0|\phi|0\rangle = \begin{pmatrix} 0 \\ v \end{pmatrix} \tag{2.7}$$

Since the Higgs field is an isospin doublet of two complex fields it has four degrees of freedom. Three of these mix with the $W^\pm$ and Z, giving them masses. The fourth degree of freedom gives rise to the prediction of a new massive scalar particle, the Higgs boson. In July 2012, the discovery of what is now referred to as a Higgs boson was announced [1, 2].

2.1.4 The hierarchy problem

There is a discrepancy between the energy scales associated with the weak interaction and that of gravity. This discrepancy is called the hierarchy problem and poses the question why the weak force is 10^{32} times stronger than gravity, or, equivalently, why the Higgs boson mass $\lesssim \mathcal{O}(1\text{ TeV})$ is so much smaller than the Planck mass $\mathcal{O}(10^{15}\text{ TeV})$. One would rather expect that the large corrections that enter into its mass term would make the mass of the Higgs boson huge. Since the fermion coupling to the Higgs boson is proportional to the fermion mass, heavy quarks, most notably the top quark, give rise to the largest corrections to the Higgs mass:

$$\Delta m_H^2 = -\frac{|\lambda_f|^2}{8\pi^2}[\Lambda_{\text{UV}}^2 + \dots], \tag{2.8}$$

[2]In the case of the Higgs mechanism, the symmetry group of the electroweak interaction, $SU(2)_L \times U(1)_Y$, is spontaneously broken down to $U(1)_{\text{EM}}$, the symmetry group of electromagnetic interactions. In the end, we are left with three massive gauge bosons (W^+, W^- and Z^0) and one massless gauge boson (the photon) – all while preserving gauge invariance.

where λ_f is the fermion coupling to the Higgs boson and Λ_{UV} is the ultraviolet cutoff – the scale up to which the Standard Model is valid. If the ultraviolet cutoff is taken to be the Planck scale, the corrections will diverge quadratically. To keep the Higgs mass below 1 TeV, counter terms need to be added by hand at each order of perturbation[3]. This way of manually inserting arbitrary numbers to achieve a goal is referred to as fine-tuning.

2.2 Beyond the Standard Model

To solve the hierarchy problem without introducing a fine-tuning, new physics at the Higgs scale is necessary. Several ideas that accomplish this have been proposed, most notably *supersymmetry* and theories with *spatial extra-dimensions*. Many of these theories predict the existence of new gauge bosons and high-mass resonances with subsequent decays into top-antitop ($t\bar{t}$) quark pairs, which indeed is the main motivation for this study. Here we will only discuss theories with extra dimensions since it will provide the basis for the analysis in Chapter 6.

2.2.1 The Randall-Sundrum model

The Randall-Sundrum (RS) model [3] is a five-dimensional theory which was conceived specifically to address the hierarchy problem. It was introduced in 1999 and received a lot of attention from theoreticians as well as experimentalists as it not only provided a satisfying solution to the problem, but also a wealth of phenomena accessible to explore at the LHC. Here we will give a short introduction to the theory of extra dimensions and the general RS idea, and then proceed with the specific case of the model where the SM gauge and fermion fields can propagate in the extra dimension (first introduced in [4, 5]).

Kaluza-Klein theory

We will begin with one of the most basic ideas of extra dimensions, known as the Kaluza-Klein scenario [6]. In this scenario, one extra spatial dimension, z, is added to our otherwise (3+1)-dimensional picture. In relativistic notation, the (4+1)-dimensional

[3] Mathematical theories that describe phenomena in nature often lack exact solutions. To do calculations, simpler versions of the complete theories, that do have exact solutions, are used instead. To correct for the difference between the theory and the measurements of the real phenomena, small corrections of the parameters in the theory are added as extra terms to the theory. These corrections are called *perturbations*. The *order* of perturbation is related to the number of times the parameters occur in the extra terms.

space-time can be written as (x^μ, z), where the index $\mu = 0, 1, 2, 3$ corresponds to the common four space-time coordinates (t, x^1, x^2, x^3). In the Kaluza-Klein scenario, the extra dimension, z, is compactified on a circle with radius R and identity between the extreme points 0 and $2\pi R$, such that $z = 0 = 2\pi R$. Thus, the picture consists of the three infinite spatial dimensions (x^1, x^2, x^3) and the $2\pi R$-periodic extra dimension z. A consequence of the geometry of the extra dimension is that the physics stays effectively four-dimensional at low energies.

Assuming the framework outlined above, we can express the field $\phi(x^\mu, z)$ of a free massless particle as a Fourier series:

$$\phi(x^\mu, z) = \sum_{n=-\infty}^{\infty} \phi_n(x^\mu) e^{ip_n^z z}, \tag{2.9}$$

where $p_n^z = n/R$ is the momentum in the extra dimension. The Fourier expansion of the field comes from the fact that p_n^z can only take discrete values in R corresponding to the mode of excitation $n \in \mathbb{Z}$. With the field written in this way, the five-dimensional equations of motion $(\partial_\mu \partial^\mu + \partial_z \partial^z)\phi(x^\mu, z) = 0$ becomes:

$$\partial_\mu \partial^\mu \phi^n(x^\mu) = \frac{n^2}{R^2} \phi^n(x^\mu), \tag{2.10}$$

giving rise to an infinite tower of Kaluza-Klein states with increasing masses $m^2 = n^2/R^2$. At energies small compared to $1/R$ only the z-independent massless zero-modes, with $n = 0$, are non-vanishing. The higher modes of the Kaluza-Klein states first start to become important at energies above $1/R$. No experiment has observed a Kaluza-Klein state, which sets a strong lower boundary on their masses of $\mathcal{O}$(TeV). There are several competing extra-dimensional scenarios (see *e.g.* [3, 7, 8]) that build upon the Kaluza-Klein idea, in which Kaluza-Klein excitations of SM particles would occur. The experimental manifestation of such excitations is model-dependent, and could *e.g.* in the production of hypothetical Kaluza-Klein excited gravitons involve an energetic gluon jet and missing energy (carried away by the graviton), or an excess production of boosted $t\bar{t}$ events in the case of Kaluza-Klein excited gluons. The latter will be studied in detail in this thesis.

The Randall-Sundrum idea

In the Randall-Sundrum model [3], the fifth dimension (also referred to as the *bulk*) is compactified on a $S_1/\mathbf{Z}_2$ orbifold; a circle whose upper and lower halves are identified (Fig. 2.1), such that $(x^\mu, \phi) = (x^\mu, -\phi)$, where ϕ is the angular coordinate of the fifth dimension. Here, S_1 denotes the circle group, and $\mathbf{Z}_2$ denotes the multiplicative group

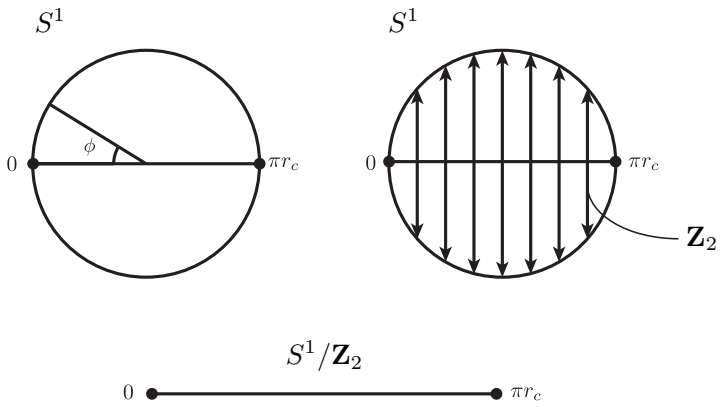

FIGURE 2.1: Illustration of the quotient space of S_1 and $\mathbf{Z}_2$; the $S_1/\mathbf{Z}_2$ orbifold. The operation of $\mathbf{Z}_2$ on the circle effectively reduces the circle to a line with a fixed point at each end [9].

$\{-1, 1\}$. With the two halves identified, the circle can be represented by a line with (orbifold) fixed points at $\phi = 0$ and $\phi = \pi$. At each of these two fixed points sit one 3-dimensional world, much like our own, known as a 3-brane. The two 3-branes are referred to as the Planck brane and the TeV brane respectively. These names reflect the energy scale prevalent on each brane. The whole picture is based on a slice of AdS_5(5-dimensional anti-de Sitter) space with length πr_c, where r_c is the compactification radius of the fifth dimension.

The choice of brane energy scales is natural; on one hand we have gravity which is associated with the Planck scale, and on the other we have the three other fundamental interactions which are associated with the weak scale. If we take the Planck scale to be the natural scale, and localize gravity on the Planck brane, then the weak scale is naturally obtained on the other brane due to the geometry of the fifth dimension. More precisely, the metric

$$ds^2 = -e^{-2kr_c\pi}\eta_{\mu\nu}dx^\mu d^\nu - r_c^2 d\phi^2 \tag{2.11}$$

of the space contains a *warp* factor, $-e^{-2kr_c\pi}$, which exponentially suppresses the energy scale as we go further away from the Planck brane. Here, $\mu = \nu = 0, 1, 2, 3$ are indices, and $\eta_{\mu\nu} = \mathrm{diag}(-1, 1, 1, 1)$ is the four-dimensional Minkowski metric. The warp factor depends on the radius, r_c, of the extra dimension and on the AdS_5 curvature scale, k. Given this metric, an examination of the four-dimensional effective action yields [5]:

$$M_{\mathrm{Pl}}^2 = \frac{M_5^3}{k}(1 - e^{-2kr_c\pi}), \tag{2.12}$$

where M_{Pl} and M_5 are the reduced four-dimensional Planck mass and the five-dimensional Planck mass respectively. From this it is realized that M_{Pl} depends only weakly on the size of the extra dimension. The physical scale, on the other hand, has a large dependence

on the extra dimension, and is given by:

$$\Lambda = M_{\mathrm{Pl}} e^{-kr_c\pi}. \tag{2.13}$$

Because of the exponential suppression factor, the energy scale of the TeV brane can be produced naturally without introducing new hierarchies.

Standard Model fields in the bulk

In the first iteration of the RS model, only the graviton is treated as a five-dimensional field. Newer iterations, however, typically promote fermions and gauge fields to freely traverse the five-dimensional bulk as well, all while keeping the Higgs field localized to the TeV brane in order to generate spontaneous symmetry breaking. In this setup, the SM fields are taken to be the zero-mode Kaluza-Klein states of the five-dimensional fields. The first excited state of the SM gluon, called the Kaluza-Klein (KK) gluon, is believed to provide one of the earliest signals of the bulk RS model since it has the largest coupling among the Kaluza-Klein particles and therefore the largest production rate [10].

The coupling between a zero-mode fermion, f, and a KK boson, $A^{(n)}$, is given by:

$$g_{f\bar{f}A^{(n)}} = g_s\sqrt{2\pi kr_c}\left[\frac{1+2\nu}{1-\epsilon^{2\nu+2}}\right]\int_{\epsilon}^{1} dz z^{2\nu+1}\frac{J_1(x_n^A z)+\alpha_n^A Y_1(x_n^A z)}{|J_1(x_n^A z)+\alpha_n^A Y_1(x_n^A z)|}, \tag{2.14}$$

where g_s denotes the strong coupling constant in the SM, $\epsilon \equiv e^{-kr_c\pi}$, and $\alpha_n^A = x_n^A e^{-kr_c\pi}$. $x_n^A = m_n^A e^{kr_c\pi}/k$, where m_n^A is the mass of the nth KK mode, are the roots to the standard Bessel functions of the first and second kind, J_1 and Y_1. The localization parameter ν is of order unity and specifies where in the bulk a fermion is located. It is the value of ν that dictates how much overlap a fermion will have with the Higgs field and subsequently what mass it will have. The following values on the localization parameter ν for different fermions are given by [10]:

$$\begin{aligned} \nu_{t_R} &\approx -0.3 \\ \nu_{Q_{3L}} &\approx -0.4 \\ \nu_{\mathrm{other}} &\approx -0.5, \end{aligned} \tag{2.15}$$

where t_R denotes the right-handed top quark and Q_{3L} the third generation quark doublet. Evaluation of Eq. 2.14 yields the fermion–KK gluon ($g^{(1)}$) couplings [10]: $g_{f\bar{f}g^{(1)}} \simeq 4g_s$ for the t_R, $g_{f\bar{f}g^{(1)}} \simeq g_s$ for Q_{3L}, and $g_{f\bar{f}g^{(1)}} \simeq 0.2g_s$ for the remaining quarks. In this model, KK gluons are produced dominantly, with subsequent decay into top-antitop quarks in 92.5% of the cases.

Chapter 3

LHC and the ATLAS Detector

3.1 The Large Hadron Collider

The Large Hadron Collider (LHC) [11] is the world's largest particle accelerator and collider. It is accommodated in a 27 km long circular tunnel buried underground at a depth of about 100 metres. The LHC is located at the European Organization for Nuclear Research (CERN) and crosses the borders of France and Switzerland, with the biggest section lying on the French side. An overview of the LHC complex is shown in Figure 3.1. The tunnel, which was constructed between 1984 and 1989, was originally housing the Large Electron-Positron Collider (LEP) [12] until it was recommissioned to house the LHC machine. At the LHC, particle beams of either protons or lead nuclei are accelerated in opposite directions in two adjacent beamlines. The beams are steered through the accelerator ring using a strong magnetic field produced by super-conducting magnets. Spread out along the ring are four locations where the beams intersect and collide. These locations each house one of the four LHC experiments: ALICE [13], ATLAS [14], CMS [15], and LHCb [16]. The work in this thesis is ATLAS-centric in that its focus is on techniques mainly used by the ATLAS experiment. Because of this, only ATLAS-specific data and specifications will be discussed from here on, ignoring the other experiments.

The LHC is the last in a cascade of accelerators that successively increase the energy of the particles. Figure 3.2 shows a schematic of the full complex of accelerators at CERN. The journey around the complex starts with decomposing hydrogen atoms into its constituents, protons and electrons, by placing a chamber full of hydrogen gas inside an electrical field. The freed protons are accelerated to 50 MeV in the linear accelerator LINAC 2. They are then fed to the Proton Synchrotron Booster (PSB) where they are accelerated to 1.4 GeV before being injected to the Proton Synchrotron where they are

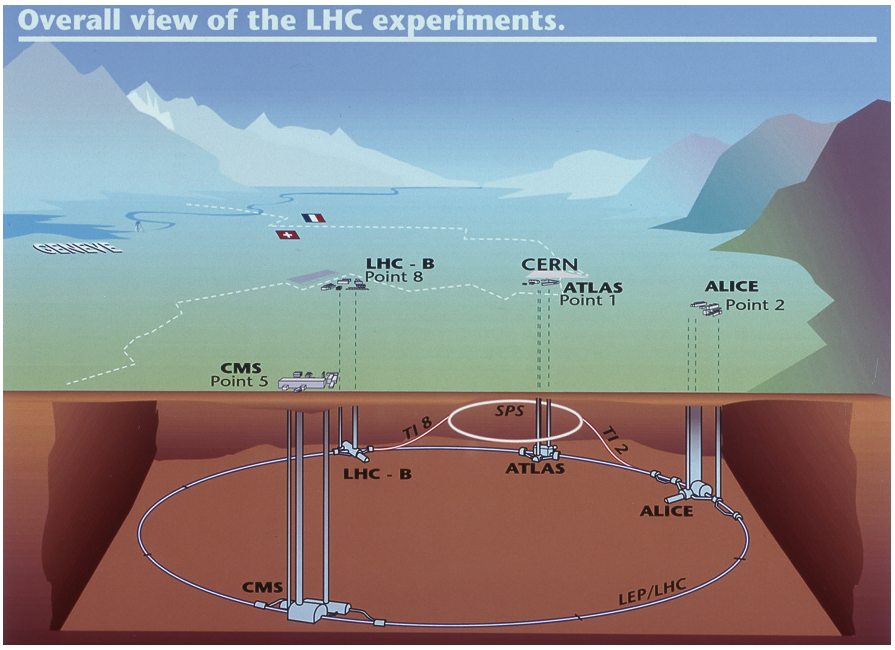

FIGURE 3.1: Overview of the LHC complex [17].

accelerated to 26 GeV. The last step before the LHC is the Super Proton Synchrotron (SPS) which further accelerates the protons to 450 GeV. At this stage the protons are ready to be injected into the LHC where they are accelerated to their final energy and left to circulate for many hours at a time. Instead of a continuous beam, the protons in the beam are lumped together into *bunches*, with each bunch containing some 10^{10} protons. Because of the bunching, the two beams will collide at the four intersections at discrete intervals, never shorter than 25 nanoseconds (ns) apart. Each bunch collision, or crossing, produces many simultaneous interactions. Already at 8 TeV, the LHC produce on average 25 interactions per crossing, a problem known as *pileup* (see Section 5.2).

3.1.1 The 2010-2012 LHC run period

From the physics point of view, the most important characteristics of a particle collider are the *energy* and *luminosity*. The LHC is designed to produce proton-proton collisions with a center of mass energy of $\sqrt{s} = 14$ TeV, or 7 TeV per beam. Due to an incident in 2008 during the initial turn on, several super-conducting magnets were damaged, and until further repairs could be made it was decided that the LHC would run at a reduced energy. Thus, during 2010 and 2011, the LHC was operated at 3.5 TeV per beam, producing $\sqrt{s} = 7$ TeV collisions. In 2012, the energy was increased to 4 TeV per beam, producing $\sqrt{s} = 8$ TeV collisions. In early 2015 the LHC is scheduled to restart for a second run after a two year break and will initially run at 6.5 TeV per beam, producing

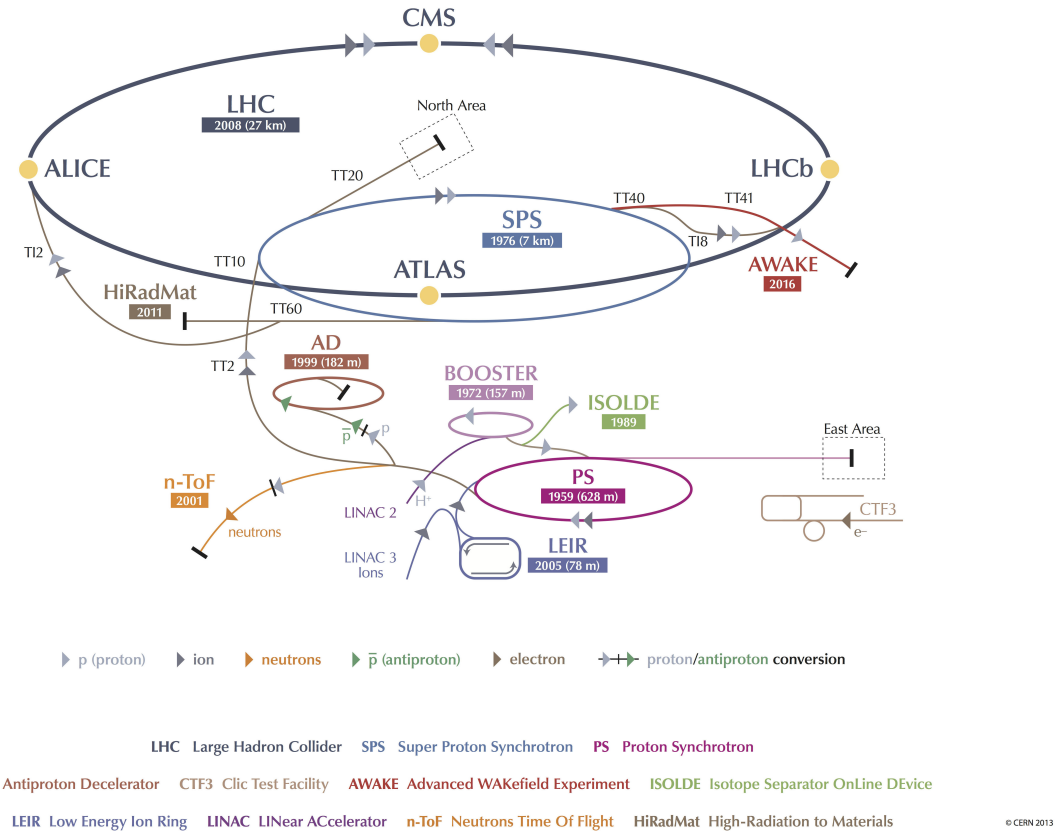

FIGURE 3.2: Schematics of the LHC injection complex. Adapted from [18].

$\sqrt{s} = 13$ TeV collisions. The design value of 14 TeV is expected to be achieved later in this run.

The luminosity, $\mathcal{L}$, also referred to as the *instantaneous luminosity*, is determined by the rate of particle collisions in a collider, and is usually expressed in units of cm^2s^{-1}. Figure 3.3 shows the instantaneous luminosity of the 2010, 2011 and 2012 data sets delivered to ATLAS. The instantaneous luminosity has increased with time and is getting close to the design value of 10^{34} $\text{cm}^{-2}\,\text{s}^{-1}$ or 10 $\text{nb}^{-1}\,\text{s}^{-1}$. Since the mean number of interactions per crossing is proportional to the instantaneous luminosity, this means that also the amount of pileup has increased.

The integral of the instantaneous luminosity over time, $L = \int \mathcal{L}\, dt$, is referred to as the *integrated luminosity*, and is a measurement of the total number of collisions collected. The integrated luminosity is often given in units of inverse femtobarns, fb^{-1}. Large integrated luminosities correspond to large number of interactions, which allows for the study of rare processes. Figure 3.4 show the integrated luminosity of the 2011 and 2012 data sets delivered to ATLAS.

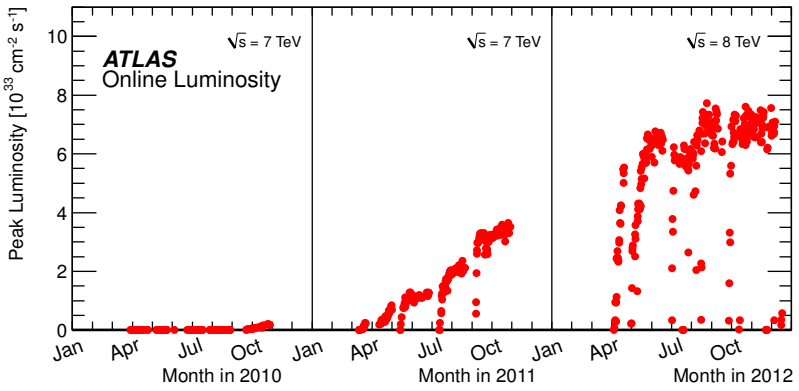

FIGURE 3.3: Instantaneous luminosity of the 2010, 2011 and 2012 data sets delivered to ATLAS [19].

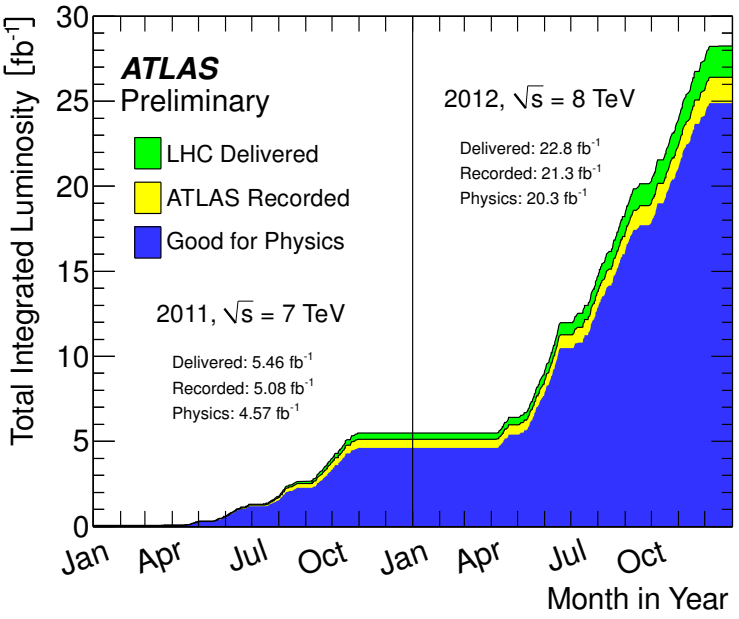

FIGURE 3.4: Integrated luminosity of the 2011 and 2012 data sets delivered to ATLAS [19].

3.2 The ATLAS Detector

The ATLAS (**A** **T**orroidal **L**HC **A**pparatu**S**) detector [14] is one of two multipurpose detectors at the LHC[1]. ATLAS is 44 meters long, 25 meters high and weighs approximately 7000 tonnes, and is centered on one of the LHC collision points 100 meters underground. The ATLAS detector is constructed in layers, and consists of three mayor subdetector systems (Fig. 3.5), each sensitive to different particles produced in the collisions.

The inner detector (ID) forms the first layer and is closest to the collision point. The ID measures the trajectories of charged particles. It consists of three subdetectors:

[1]The other one being CMS.

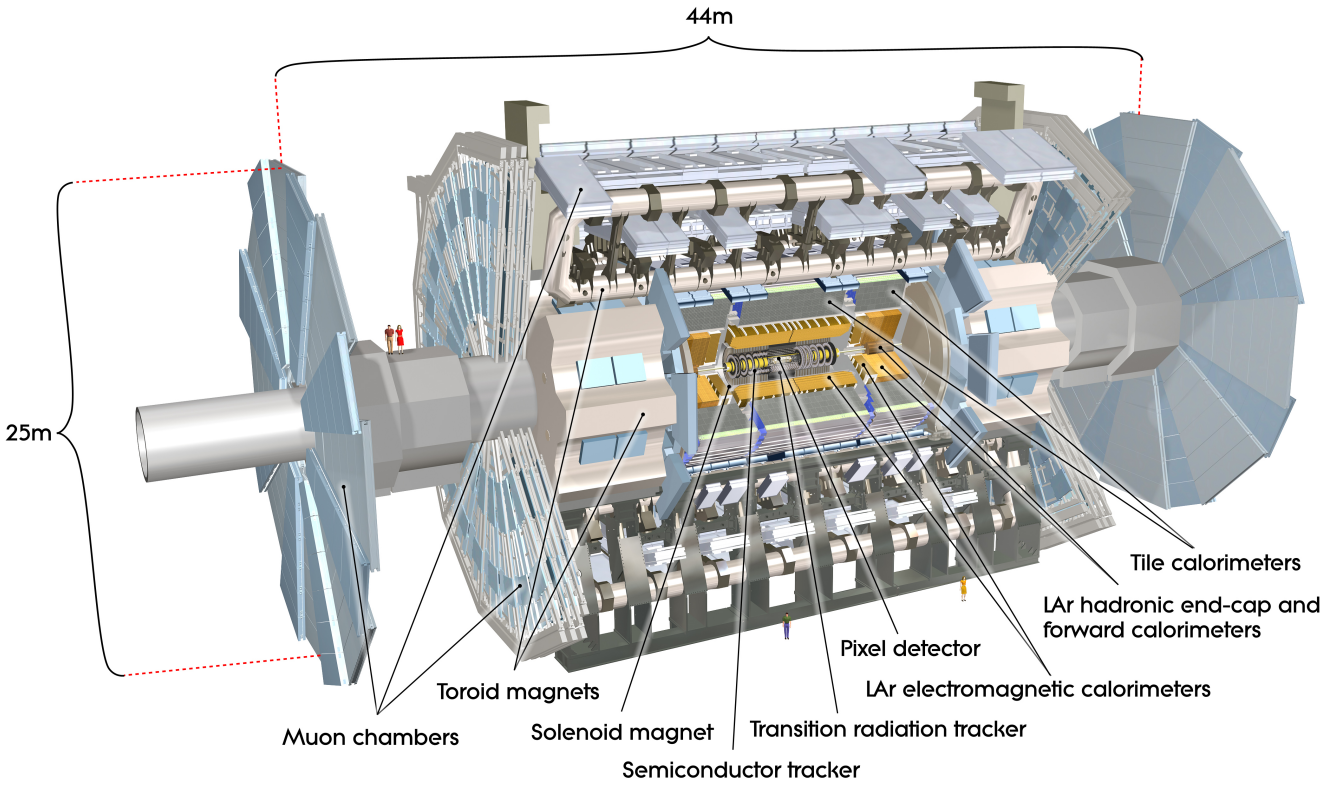

FIGURE 3.5: The ATLAS detector and subsystems [20].

The Pixel Detector, the Semiconductor Tracker (SCT), and the Transition Radiation Tracker (TRT). The whole ID is embedded in a 2 Tesla magnetic field provided by the solenoid magnet. The second layer consists of the calorimeter system, which measures the energy of electrons, photons and hadrons. The calorimeter system is composed of the liquid argon electromagnetic calorimeters, the tile calorimeters, the liquid argon hadronic end-cap calorimeters, and the forward calorimeters. The calorimeter system allows for the reconstruction of particles and jets through the energy that they depose in the calorimeter, and is thus a central component for jet analysis. In the outermost layer is the muon system, designed to detect muons and measure their trajectories. It consists of muon chambers operating in a magnetic field provided by the toroidal magnets.

The coordinate system used in ATLAS is defined with the origin at the interaction point in the center of the detector. The z-axis runs along the beam line, the x-axis is along the horizontal, with positive pointing from the interaction point to the center of the LHC ring, and the y-axis is along the vertical, with positive pointing to the surface of the earth. The xy plane is referred to the transverse plane since it is perpendicular to the beam line. Momentum measured in the transverse plane is called transverse momentum, and is denoted by p_{T}. The azimuthal angle ϕ is defined in the xy plane and is measured

from the x-axis. The polar angle θ is defined as the angle from the positive z-axis, and is often expressed in terms of pseudorapidity, defined as $\eta = -\ln\tan(\theta/2)$.

Chapter 4

Algorithms and Identification of Top Quarks

4.1 Jet Algorithms

As a consequence of color confinement, it is not possible to directly observe colored objects (quarks and gluons). Instead, algorithms that construct physics objects – jets – out of the resulting sprays of particles after hadronization, are used. These *jet algorithms* can be split into two broader classes of algorithms: Cone algorithms and sequential recombination algorithms. Cone algorithms work in a "top-down" fashion, centered around the idea that QCD branching (*i.e.* the splitting of a parton into a cascade, or shower, of new partons) and hadronization does not substantially change the overall energy flow of an event. Specifically, the energy flow can be thought of as forming a cone, and the role of the cone algorithm is to find coarse regions of energy flow (or cones) and label them as jets. Sequential recombination algorithms, on the other hand, take a "bottom-up" approach by iteratively recombining the closest pair of particles according to some distance measure.

Common for all jet algorithms is that they are always associated with a recombination scheme, which is basically the instructions for how two particles should be combined into one and, specifically, what momentum this new particle should be assigned. Nowadays, the most commonly used recombination scheme is the E-scheme, which simply defines the merging of two particles into one as the addition of their 4-vectors [21].

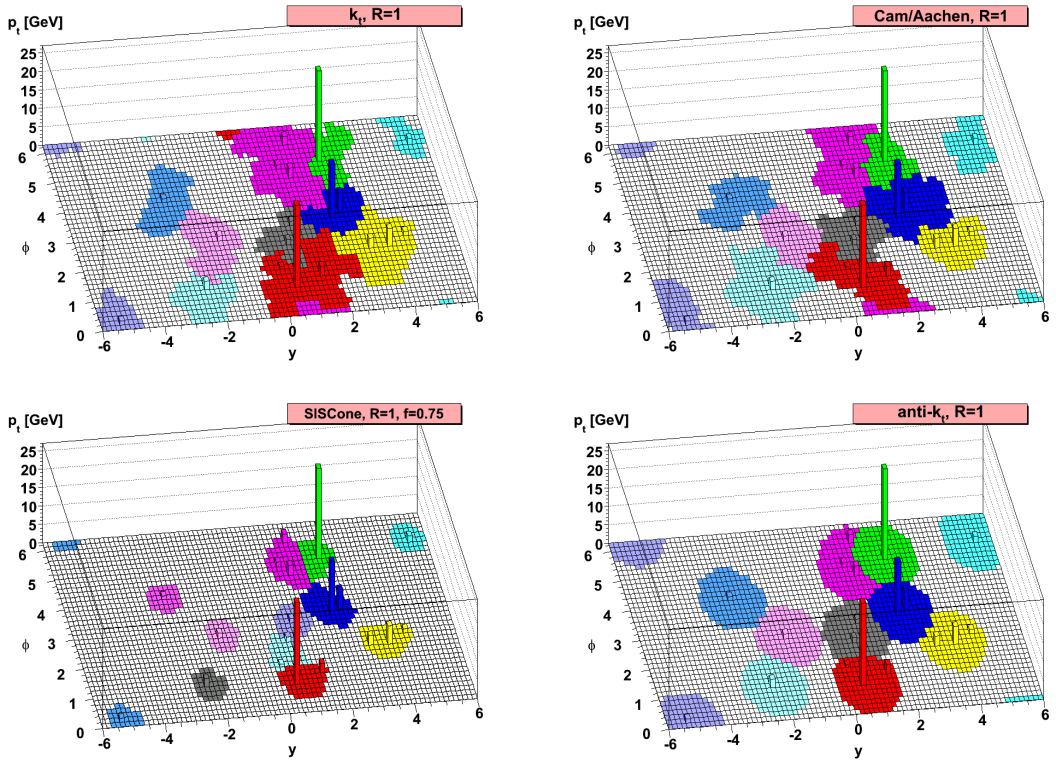

FIGURE 4.1: Illustration of jet shapes in the same event, using different algorithms [22].

4.1.1 Inputs to Jet Reconstruction

Depending on which type of input a jet algorithm is applied on, the resulting jets can be divided into three categories accordingly [23]:

- **truth jets** – in the case of Monte Carlo[1] simulations, truth jets are built from the four-vector of stable particles, where the notion "stable particle" has to be defined according to certain criteria, *e.g.* a lifetime exceeding 10 ps excluding and excluding muons and neutrinos,
- **track jets** – when input is charged particle tracks in a detector, originating from the primary hard scattering vertex,
- **calorimeter jets** – when input is energy depositions in the calorimeters of an experiment.

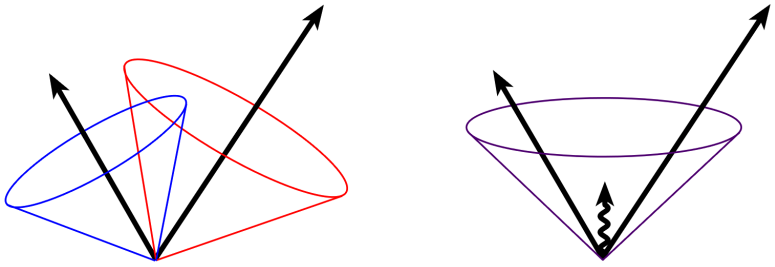

FIGURE 4.2: Illustration of infrared un-safety. Two separate partons (left) are merged into one (right) due to emission of soft radiation.

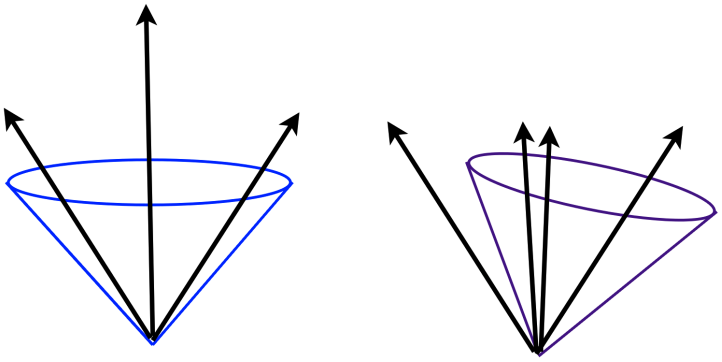

FIGURE 4.3: Illustration of collinear un-safety. A hard parton (left) is split into two partons (right) separated by a small angle due to a collinear splitting.

4.1.2 Infrared and Collinear Safety

When clustering jets, two problems of a theoretical nature need to be considered:

Infrared and collinear (IRC) safety. IRC safety is the property that if an event is modified by adding soft emission (where "soft" means an energy and momentum much smaller than the masses and energies characteristic of the event in question) or collinear splitting (the splitting of a hard parton into two partons separated by a small angle), the set of hard jets that are found in the event should remain unchanged. As a basic example of infrared (IR) safety (Fig. 4.2), consider two adjacent hard partons that initially would end up as two separate jets after clustering. Now, adding soft radiation between the two partons could in the case of an IR unsafe algorithm instead merge the two partons into one jet. An IR safe algorithm on the other hand, should be insensitive to the added soft radiation and thus keep the two jets.

As an example of collinear splitting, think of a quark emitting a gluon at a small angle. While a collinear safe algorithm is insensitive to the gluon emission of the quark, and

[1]Monte Carlo refers to a technique where repeated random sampling is used to obtain a numerical result. Typically, one generates many events randomly according to a distribution given by a model of the problem at hand.

combines the quark and the gluon into one jet, a collinear unsafe algorithm would instead divide the two partons into two jets (Fig. 4.3).

Infrared and collinear safety is also of concern in fixed-order perturbative QCD calculations, which is one of the main tools for making accurate Standard Model predictions at high-energy colliders. In perturbative calculations, soft radiation and collinear splitting give rise to divergent tree-level matrix elements and divergent loop matrix elements respectively. The two sources of divergence enter with opposite sign and for an IRC safe jet algorithm they cancel out, but for an IR unsafe jet algorithm the tree-level splittings may result in one set of jets, while the loop diagrams may result in another. This would break the cancellation and lead to infinite cross sections [21].

To compare experimental results to the expectations at hadron-level, IRC safe algorithms need to be used or the experimental results are only valid for comparison to theoretical predictions to a certain order after which the algorithm becomes IRC unsafe [21].

4.1.3 Sequential Recombination Algorithms

Sequential recombination algorithms try to reverse the process of parton showering (*i.e.* the successive QCD branching leading to a cascade of radiation). The core idea behind such algorithms lies in the use of a metric, or distance function, to determine which particles to cluster. How the distance parameter is chosen varies between the different algorithms. There are many sequential recombination algorithms to choose from. The ones most commonly used at hadron colliders are the inclusive k_t, Cambridge/Aachen and anti-k_t algorithms [22, 24, 25]. As we shall see, these three algorithms are closely related in their formulation.

We start by defining a distance measure d_{ij} between two particles, i, j, such that [22]:

$$d_{ij} = \min(p_{ti}^{2p}, p_{tj}^{2p}) \frac{\Delta R_{ij}^2}{R^2}, \qquad \Delta R_{ij}^2 = (y_i - y_j)^2 + (\phi_i - \phi_j)^2, \tag{4.1a}$$

$$d_{iB} = p_{ti}^{2p}, \tag{4.1b}$$

where p_{ti} is the transverse momentum of particle i (with respect to the beam direction, z), $y_i = \frac{1}{2} \ln \frac{E_i + p_{zi}}{E_i - p_{zi}}$ and ϕ_i are the rapidity[2] and azimuthal angle of particle i, d_{iB} is the distance between particle i and the beam, and R is a parameter of the function related to the jet radius. The parameter p is usually set to -1, 0, or 1 and depending on its value, different behaviors of the clustering is obtained.

[2] Although pseudorapidity could also be used, rapidity is preferred since differences in rapidity are invariant under boosts along z, which means that the measurement can safely be made in the laboratory frame.

A clustering algorithm can then be defined by the procedure:

1. For each pair of particles i, j work out the k_t distance and beam distance according to eq. (4.1).
2. Find the minimum of all the d_{ij} and d_{iB}.
3. If the minimum is a d_{ij}, merge particles i and j into a single new particle.
4. If instead the minimum is a d_{iB}, declare i to be a final-state jet, and remove it from the list of particles[3]. Return to step 1.
5. Stop when no particles remain.

If the parameter p in Eq. (4.1) is set to 1, we retrieve the distance measure for the k_t algorithm:

$$d_{ij} = \min(p_{ti}^2, p_{tj}^2)\frac{\Delta R_{ij}^2}{R^2}, \qquad \Delta R_{ij}^2 = (y_i - y_j)^2 + (\phi_i - \phi_j)^2, \tag{4.2a}$$

$$d_{iB} = p_{ti}^2, \tag{4.2b}$$

Due to the positive exponent of p_{t_i} and p_{t_j}, the k_t algorithm favors clusterings that involve soft particles. If instead p is set to -1, an algorithm which favors clusterings with hard particles emerges. The clustering of this algorithm is inverse to that of the k_t algorithm, and is aptly named the anti-k_t algorithm. Both of these the algorithm proceeds in the way specified above.

Finally, we get the C/A algorithm by choosing $p = 0$, which leads to:

$$d_{ij} = \frac{\Delta R_{ij}^2}{R^2} \quad \text{and} \quad d_{iB} = 1. \tag{4.3}$$

The C/A algorithm recombines the pair of particles with the smallest distance ΔR_{ij} in the $y - \phi$ plane, and repeats the process until all objects are separated by a $\Delta R_{ij} > R$. The set of particles that are left at the end of the procedure are then the jets.

4.1.4 Jet Grooming

Jet grooming is the common term for jet analysis techniques to remove constituents of an existing jet, to obtain a new jet with properties/observables which more clearly reveal

[3]Note that, however unlikely, a one-particle jet is possible (*e.g.* if in the first iteration of the algorithm, d_{iB} is the smallest distance), and would at detector level correspond to a single cluster. However, it should be emphasised that a jet is purely an algorithmic construction; it is not identical to a hadronic shower from a parton.

its origin. Pruning [26], trimming [27] and (mass-drop) filtering [28, 29] are examples of such techniques. Of these three, only mass-drop filtering is relevant to us in this work, and so we will keep our discussion to this method.

4.1.4.1 Mass-drop filtering

Mass-drop filtering [28, 29] is an iterative decomposition procedure to search for boosted heavy-particle decay. It is only applied to C/A jets as they provide an angular-ordered hierarchical structure (clustering history) for the clustered jets – a useful property when searching for hard splittings within a jet.

The mass-drop filtering algorithm proceeds in the following way:

1. Define a jet j with the C/A algorithm for some radius R.
2. Undo the last stage of the clustering (*i.e.* the last particle recombination in the clustering history) and break the jet j into two subjets j_1, j_2, where j_1, j_2 are ordered such that $m_{j_1} < m_{j_2}$. Here it is required that the mass m_{j_1} of the jet j_1 after the splitting is significantly lower than the mass m_j of the original jet j: $m_{j_1} < m_j\mu$, where μ is a parameter of the algorithm. It is also required that the energy sharing between the two jets j_1, j_2 after the splitting is relatively symmetric, approximated by the requirement that

$$\frac{\min[(p_{tj_1})^2, (p_{tj_2})^2]}{(m_j)^2} \times \Delta R^2_{j_1,j_2} > 0.09,$$

   where the value of 0.09 has been shown to be optimal for identifying two-body decays [28] (the type of decays that are of interest in this thesis). This requirement forces both subjets to carry some significant fraction of the momentum of the original jet, where in general, the p_{T} of the softer of the subjets is at least 15 % of that of the original jet.
3. If the requirements in the previous step are satisfied, the two subjets are reclustered using the C/A algorithm with radius parameter $R_{\mathrm{filt}} = \min[0.3, \Delta R_{j_1,j_2}/2]$.Otherwise, the jet is discarded.

In the mass-drop filtering procedure, the mass-drop is key for the background elimination, while the filtering is necessary to obtain a good mass resolution on the signal [28].

4.2 Identifying top quarks

4.2.1 The top quark

The top quark belongs to the third generation of quarks and is by far the heaviest of them all with a mass of 173 GeV[4] [30]. Because of its large mass, the top quark has a large coupling to the electroweak symmetry breaking sector. This has led to a long lasting speculation whether the top quark itself may play a special role in the electroweak symmetry breaking [31]. The top quark is also interesting for another reason. It is expected to couple strongly to new physics and thus act as a natural probe in many scenarios for physics beyond the SM. In several models, new particles predicted to exist decay predominantly into top quark pairs (see *e.g.* [10]).

4.2.2 Top quark production

At hadron colliders, top quark production is dominated by top-antitop ($t\bar{t}$) pair production through the strong interaction and single top production through the weak interaction. The main leading order (LO) strong interaction processes responsible for the $t\bar{t}$ production are gluon-gluon scattering (Fig. 4.4) and quark-antiquark annihilation (Fig. 4.5).

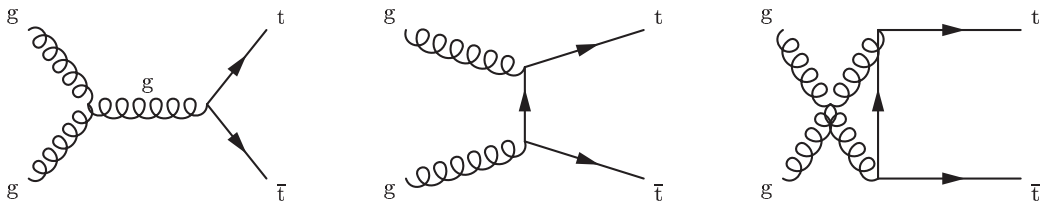

FIGURE 4.4: Feynman diagrams for the production of $t\bar{t}$ events via gluon-gluon fusion.

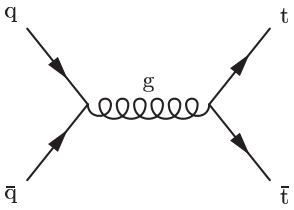

FIGURE 4.5: Feynman diagram for the production of $t\bar{t}$ events via quark-antiquark annihilation.

[4]Compare with the gold nucleus which weighs 182.7 GeV

4.2.3 Top quark decay

The top quark is the only quark that is unable to form bound states with other quarks and gluons. This is a consequence of its short lifetime which is in the order of 10^{-24} s. Since the timescale of the strong interaction, responsible for the formation of hadrons, is of the order 10^{-23} s, the top quark simply decays before it has the chance to hadronize. The top quark decays almost exclusively into a W boson and a b-quark, hence it is the decay of the W boson that characterizes the decay (only the W decays further, while the b-quark hadronizes and forms two jets of hadronic particles). The "top quark" thus has two modes of decay: leptonic or hadronic. In the leptonic decay, the W decays into a charged lepton and its associated neutrino, and the final state thus consists of a b-quark, a charged lepton, and its associated neutrino, $t \to W^+b \to l^+\nu_l b$. In the hadronic decay, the W decays into a quark-antiquark pair, and the final state thus consists of a b-quark and a quark-antiquark pair , $t \to W^+b \to q\bar{q}b$.

4.3 Boosted tops

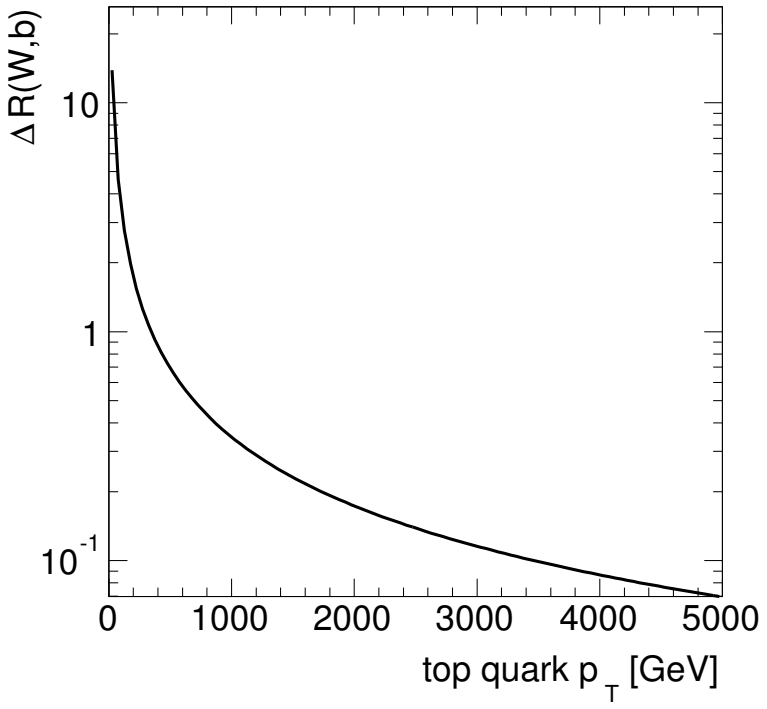

FIGURE 4.6: Approximation of the opening angle between top quark decay products W and b as a function of the transverse momentum of the top quark.

Up until the LHC era, the study of top-antitop final states has primarily been of $t\bar{t}$ produced at rest. In the case of such low-energetic top quarks, the decay products form

clearly separated jets and the detection of these jets has been the basis in algorithms designed to tag top quarks. However, as the energy is increased, heavier particles, such as the Kaluza-Klein gluon, could be produced and subsequently decay into $t\bar{t}$ pairs with high transverse momentum, $p_{\mathrm{T}} \sim 0.5 M_{g_{KK}}$. The decay products of such energetic tops will be highly collimated, with jets lying close to each other or even overlapping. Algorithms relying on the detection of clearly separated jets will thus fail and new techniques, such as jet substructure, are needed for the identification of top quarks. The angular separation, ΔR, between jets formed from the decay products of a particle with mass m and transverse momentum p_{T} scales as [32]:

$$\Delta R \sim \frac{2m}{p_{\mathrm{T}}}. \tag{4.4}$$

Fig. 4.6 show ΔR as a function of top quark p_{T}.

4.4 The HEPTopTagger

Top taggers are algorithms designed to optimize the identification of top quarks. The HEPTopTagger (Heidelberg-Eugene-Paris) [33] is one such in a growing range of top taggers. It is designed to optimize the selection of hadronically decaying, moderately boosted top quarks (*i.e.* top quarks with transverse momentum $m_t \lesssim p_T \lesssim 5m_t$ and a hadronically-decaying W boson daughter) over a large multi-jet background. The method (Fig. 4.7) uses a variant of the mass-drop filtering technique described above [33, 34]:

1. Define a jet j with the C/A algorithm for some radius R.

2. Undo the last stage of the clustering process in the previous step by breaking the jet j into two subjets j_1, j_2, where j_1, j_2 are ordered such that $m_{j_1} < m_{j_2}$. The mass-drop criterion $m_{j_1} < m_j \mu$, where μ is a parameter of the algorithm, determines if j_1 and j_2 are kept; if the condition is not met, only j_1 is kept. Each subjet j_i is then further decomposed (if $m_{j_i} > m_{\mathrm{cut}}$, where m_{cut} is the largest mass allowed for the subjet j_i) or added to the list of relevant substructures. When the de-clustering procedure is complete, there must exist at least three hard subjets, otherwise the jet j is discarded.

3. Iterate over all combinations of three subjets (triplets) and filter with resolution $R_{\mathrm{filter}} = \min(0.3, \Delta R_{jk}/2)$, *i.e.* recluster the constituents of the triplets using the C/A algorithm with radius parameter $R = R_{\mathrm{filter}}$. The parameter ΔR_{jk} is the minimum separation between all possible pairs in the current triplet.

4. Calculate the invariant mass of the four-vector determined by summing the five hardest constituents (if less than five, use all) of the triplets that have been filtered, and select the triplet with mass closest to the top quark mass, m_t. Discard all other triplets.

5. Construct exactly three subjets j_1, j_2, j_3, ordered by p_T, by applying the C/A algorithm to the five hardest constituents of the selected triplet. Accept the set of subjets j_1, j_2, j_3 as a top candidate if any of the following conditions are satisfied:

$$
\begin{aligned}
&0.2 < \arctan\frac{m_{13}}{m_{12}} < 1.3 \qquad \text{and} \quad R_{\text{min}} < \frac{m_{23}}{m_{123}} < R_{\text{max}} \\
&R^2_{\text{min}}\left(1+\left(\frac{m_{13}}{m_{12}}\right)^2\right) < 1-\left(\frac{m_{23}}{m_{123}}\right)^2 < R^2_{\text{max}}\left(1+\left(\frac{m_{13}}{m_{12}}\right)^2\right) \quad \text{and} \quad \frac{m_{23}}{m_{123}} > 0.35 \\
&R^2_{\text{min}}\left(1+\left(\frac{m_{12}}{m_{13}}\right)^2\right) < 1-\left(\frac{m_{23}}{m_{123}}\right)^2 < R^2_{\text{max}}\left(1+\left(\frac{m_{12}}{m_{13}}\right)^2\right) \quad \text{and} \quad \frac{m_{23}}{m_{123}} > 0.35
\end{aligned}
\tag{4.5}
$$

   with $R_{\text{min}} = (1 - f_W)m_W/m_{\text{top}}$ and $R_{\text{max}} = (1 + f_W)m_W/m_{\text{top}}$, where f_W is a resolution variable (taken to be 15 in [33]). The parameters m_W and m_{top} are the experimentally established masses of the W boson and the top quark, and m_{123} and m_{ij} are the total invariant mass of the three subjets and the invariant mass formed from combinations of two of the three C/A jets, j_1, j_2, j_3, respectively.

The studies presented in this thesis use the HEPTopTagger algorithm with the default parameter values as given in the original source code[5]. Notably, this means that $\mu = 0.8$ and $m_{\text{cut}} = 30$ GeV are used here. These parameters can be optimized for a given analysis (see *e.g.* [34]), however such optimizations falls outside the scope of this thesis.

[5]Source code can be found at:
http://www.thphys.uni-heidelberg.de/~plehn/index.php?show=heptoptagger&visible=tools

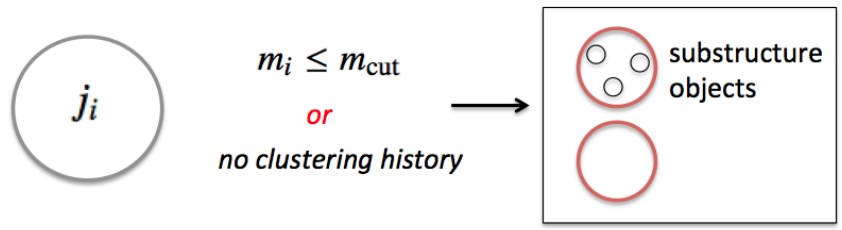

(A)

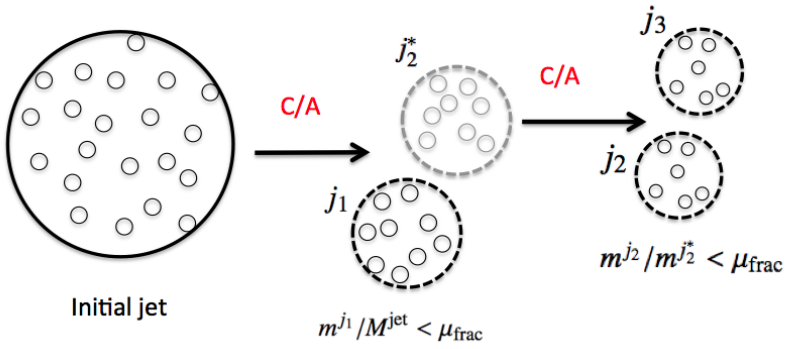

(B)

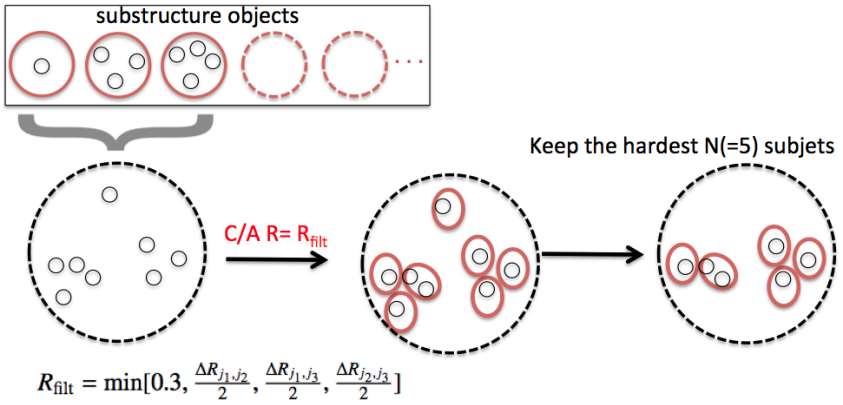

(C)

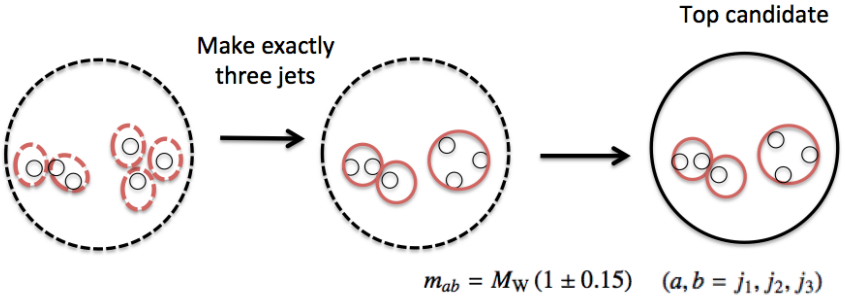

(D)

FIGURE 4.7: Illustration of the HEPTopTagger procedure [34].

Chapter 5

Analysis: Method and Performance

As we have seen in the previous chapter, the way in which particles are clustered into jets varies significantly between different algorithms. For k_t, particles with lowest transverse momentum are clustered first, while the opposite is true for anti-k_t. C/A works independently of the transverse momentum and clusters particles only based on their relative distance in $y - \phi$. As a result, the set of jets that are found in an event can, and often will, differ depending on which jet algorithm is used. In particular, it is the sensitivity to non-perturbative effects such as hadronisation and underlying event (*i.e.* all particles from a single particle collision except those from the process of interest) contamination that changes the outcome of different jet algorithms. The ATLAS collaboration presently uses the anti-k_t algorithm with radius parameter $R = 0.4$ and $R = 0.6$ as the default jet definition in jet analyses.

This chapter presents a study on how the HEPTopTagger algorithm performs on boosted jets that have undergone two clustering stages. In the first stage, all available final-state particles are clustered into jets using the anti-k_t algorithm. This yields jets with well-defined shape and area, but with the drawback that they, for the reasons discussed earlier, are not compatible with the HEPTopTagger. In the second stage, the contents of these jets are reclustered on a jet-by-jet basis using the C/A algorithm. This produces new jets with the necessary clustering history to be used together with the HEPTopTagger.

The aim of this study is to answer two main questions:

1. Can the HEPTopTagger be used successfully on jets first clustered with the anti-k_t algorithm?

2. Is it possible to tag highly boosted top quarks ($p_{\mathrm{T}} > 1$ TeV) with the HEPTopTagger?

5.1 Monte Carlo simulation

5.1.1 PYTHIA 8

In this study we rely exclusively on Monte Carlo simulations of proton–proton (pp) collisions. The Monte Carlo *event* generator used is PYTHIA8 version 8.180, which simulates high-energy collisions at leading order. With *event* we mean the hard interaction between two particles (in our case, two protons) and the subsequent scattering and production of new particles.

5.1.2 Event generation

Two sets of processes are simulated: 1) SM $t\bar{t}$ decaying into $W^{\pm}$ bosons and $b\bar{b}$ quarks via gluon-gluon and quark-antiquark scatterings, and 2) hard QCD processes, excluding $t\bar{t}$ production. The $W^{\pm}$ in the $t\bar{t}$ process are required to decay hadronically. All events are generated at center of mass energy $\sqrt{s} = 14$ TeV, and using the leading-order (LO) parton distribution function (pdf) CTEQ5L [35]. The $t\bar{t}$ events are used to quantify the efficiency of the top tagger, while the QCD sample is used to test the tendency of the top tagger to falsely tag jets originating from light gluons and quarks.

Since our interest is in boosted top quarks, events are generated with a phase space ($\hat{p}_{\mathrm{T}}$) greater than 300 GeV. Twelve sets of events are produced, ranging from 300 GeV to 5 TeV.

5.1.3 Particle Selection

Only final-state particles with pseudorapidity $\eta \leq 4.5$ are considered for the analysis. In the event generation, particles with nominal proper lifetime $\tau_0 > 1000$ mm/c are considered stable. Furthermore, muons and neutrinos are neglected for selection to the analysis since they will not be detected in the calorimeters (and in the case of the neutrino, not at all).

5.2 Detector effects

Spatial resolution

Detector resolution is an important limiting factor when it comes to identifying the decay products of highly boosted top quarks. All detectors have a finite spatial resolution,

related to their *granularity*. A high granularity results in a high resolution and vice versa. The granularity that is of interest to us, is that of the calorimeter detector which is essential for measuring jets. When not applied on particle level, the HEPTopTagger is designed to be used on hadronic calorimeter cells. The cell size of the ATLAS calorimeters as given in coordinates of pseudorapidity and azimuth ranges from $\Delta\eta \times \Delta\phi = 0.025 \times 0.025$ to 0.2×0.2 in $|\eta| > 2.5$.The cell size of the hadronic calorimeter of ATLAS is typically 0.1×0.1 in $|\eta| < 1.7$ (where most of the high-p_{T} jets are in the detector). Thus, to separately resolve all three jets from a hadronic top quark decay, without the risk of two jets hitting the same cell, the smallest separation $\Delta R = \sqrt{(\Delta\eta)^2 + (\Delta\phi)^2}$ between any of the jets need to be larger than 0.1.

To simulate the effect of calorimeter granularization, we let each particle from the event pass through a grid with 200×100 cells of size 0.1×0.1 in (η, ϕ). The grid is set up in such a way that each cell corresponds to a set of integer coordinates $(\eta_{\mathrm{cell}}, \phi_{\mathrm{cell}})$. To decide in which cell to add an incoming particle, the procedure divides the particle's η and ϕ values with the cell size (0.1) and checks which cell coordinates correspond to the resulting fractions. In this way, a particle with *e.g.* $(\eta, \phi) = (1.5, 2.5)$ is added to cell (15,25), and so forth.

Energy resolution

Aside from the spatial resolution, a calorimeter also has a finite energy resolution, σ_E/E, given by:

$$\frac{\sigma_E}{E} = \frac{A}{\sqrt{E}} \oplus \frac{B}{E} \oplus C. \tag{5.1}$$

Here the coefficients, A, B and C are respectively attributed to fluctuations inherent in the development of showers, and by calibration and instrumental limits. The coefficients vary for electromagnetic showers and for hadronic showers since less energy can be recorded from hadronic interactions (in a non-compensating hadronic calorimeter).

In the ATLAS detector, the energy resolution for electrons and photons is:

$$\frac{\sigma_E}{E} = \frac{10\%}{\sqrt{E}} \oplus \frac{170\,\mathrm{MeV}}{E} \oplus 0.7\%. \tag{5.2}$$

The similar resolution for hadrons is:

$$\frac{\sigma_E}{E} = \frac{52.9\%}{\sqrt{E}} \oplus 5.7\%. \tag{5.3}$$

Since the electronic noise, corresponding to the B-coefficient, is negligible, its term is not used for this parametrization [36]

The *smearing* effect of the energy distribution that the energy resolution imposes, is simulated by picking a random number $\bar{E}$ from a Gaussian distribution with mean $\mu = E_{\text{particle}}$ and standard deviation σ given by (5.3) and (5.2) (depending on if the particle is a hadron or not), and replacing the energy of the particle four-momentum with $\bar{E}$, such that $(\mathbf{p}, E_{\text{particle}}) \to (\mathbf{p}, \bar{E})$.

Pileup

At the LHC, the general term *pileup* usually refers to the additional proton-proton collisions, other than the one of interest, that occurs at every *bunch* crossing, and is one of the biggest challenges for physics analysis with jets. The pileup background consists of two main components: in-time pileup and out-of-time pileup. In-time pileup refers to the additional $p\bar{p}$ interactions that occur in the same *bunch* crossing, and result in additional signals in the calorimeters. Out-of-time pileup refers to the additional $p\bar{p}$ interactions in bunch-crossings right before and after the collision of interest, that can still affect the signal due to latency in the detector's electronics.

The mean number of inelastic $p\bar{p}$ interactions per bunch crossing, denoted by $\langle\mu\rangle$, is given by [37]:

$$\langle\mu\rangle = \frac{L \times \sigma_{\text{incl.}}}{N_{\text{bunch}} \times f_{\text{LHC}}}, \tag{5.4}$$

where L is the instantaneous luminosity, $\sigma_{\text{incl.}}$ is the total inelastic $p\bar{p}$ cross-section, N_{bunch} is the number of bunches, and f_{LHC} is the frequency of bunch crossing in the LHC. In 2012, there were on average $\langle\mu\rangle \approx 20.7$ interactions per bunch crossing [37].

In this study, pileup is simulated by the inclusion of N extra events per main event (background or signal) where N is drawn from a Poisson distribution with expected value $\langle\mu\rangle = 20$.

5.3 Analysis Strategy

The performance of the two-stage clustering procedure outlined above is compared with the ordinary HEPTopTagger procedure where only the C/A algorithm has been used to produce jets. For both procedures, only particles that have passed the selection criteria above are used in the jet finding. The two procedures are as follows:

- The two-stage clustering procedure starts with clustering the particles into jets with the anti-k_t algorithm with radius parameter R =0.4, 0.6 and 1.0. From the jets formed, only the ones with p_{T} larger than 200 GeV are kept.

The constituents of each jet are then clustered into new jets with the C/A algorithm, with the same radius parameter as in the previous step. Although the standard procedure usually uses "fat" jets with radius larger than $R = 1.0$ in order to capture the complete decay at low energies, our interest in highly boosted tops makes it possible to use a smaller radius.

- In the standard procedure jets are clustered directly with the C/A algorithm. To make the comparison between the two procedures easier, the same values of the radius parameters used in the two-stage clustering procedure are used here as well.

5.4 Results

A common measure of the performance of a tagger is its *efficiency* and *fake rate*. The efficiency is defined as the number of tagged top quarks divided by the number of top quarks in the sample, and is measured as a function of transverse momentum of the generated top quark. Similarly, the fake rate is defined as the probability to tag a jet originating from light quarks (u, d, s, c, b) or gluons (*i.e.* the number of tagged jets divided by the number of QCD events in the sample). As in [34], the fake rate is measured as a function of the leading anti-k_t jet with $R = 0.4$, since it provides a measure for the available energy in the event and can be easily comparable between different tagging approaches.

No detector effects

In Fig. 5.1 the efficiency and fake rate for the two top tagging procedures are shown in the case when no detector effects are considered, representing the ideal case of a perfect detector. The three cases with jet radii $R = 0.4, 0.6$ and 1.0 are shown. For $R = 0.4$ jets, the efficiency starts to increase sharply around 750 GeV and reaches a plateau of $\sim$ 35% around the 1.5 TeV mark. Jets formed from decay products of the top quark have a separation of $\Delta R = 0.4$ around 900 GeV (see Fig. 4.6), which is where we would expect the sudden increase to happen. As expected, the fake rate starts to increase around the same p_{T} as the efficiency and remains stable at below 4% percent within uncertainties. The stabilization, however, occurs slightly later than for the efficiency. Note the different scales of the efficiency plots and the fake rate plots.

The efficiency for the $R = 0.6$ and 1.0 jets follows the same pattern as the smaller jets, although with the sudden increase occurring earlier in the spectrum. The fake rates flattens out at the same time as the efficiency, and remains around 4% and just below 6%

respectively. Although the efficiencies stabilize around nearly the same values ($\sim 35\%$) for all three R-values, the fake rates for the $R = 0.6$ and, especially, the 1.0 jets, are higher than the $R = 0.4$. This indicates that for searches above 1.5 TeV, it would be beneficial from a signal-to-background point of view to use $R = 0.4$ and 0.6 jets rather than 1.0.

Comparing the two tagging procedures described in section 5.3 (hereafter respectively referred to as anti-k_t + C/A and C/A), it is seen that for all three R-values, the efficiencies and fake rates for anti-k_t + C/A and C/A coincide over the whole p_{T} spectrum. In the $R = 0.4$ case, we observe some fluctuations in the fake rate between the two procedures, but these are within uncertainties. This general appearance, as we will see, remains the same in all cases including detector effects as well.

Including a grid

The performance when a grid is included in the simulation is shown in Fig. 5.2. As is expected, the efficiency starts to roll off at higher p_{T} due to individual jets no longer being resolved in the "detector". However, the point at which this happens varies for the different R-values. The efficiencies for the $R = 0.4$ and 0.6 jets peaks at around 1.5 TeV after which it decreases. For $R = 1.0$ the peak instead occurs earlier, around 1.2 TeV.

The fake rates are in general lower than in the case with no detector effects, about 2% above 1.5 TeV for $R = 0.4$. For $R = 0.6$ the fake rate peaks around 4% at 1.5 TeV and then decreases to about 2% at high p_{T}. The $R = 1.0$ fake rate has a clear peak around 1.5 TeV which then decreases to about 2% at high p_{T}.

Including smearing

From comparing Figs. 5.3 and 5.1 it can be seen that restrictions on energy resolution of the detector do not affect the performance noticeably.

Including pileup

The addition of pileup has a drastic effect on the fake rate of the $R = 1.0$ jets, as can be seen in Fig. 5.4 (F). (Note the scale of the y-axis). At low p_{T} the fake rate is more than 30%, which is comparable to the efficiency which is about 40% at the same p_{T}. The fake rate then decreases abruptly to about 15% at 1 TeV after which it remains stable within uncertainties. The efficiency also decreases, from 40% at 500 GeV to about 25% at 1.5 TeV and then further to 20% at 2.5 TeV. Note that the statistical uncertainties are

smaller in this specific case due to the larger number of measured events. For $R = 0.6$ the fake rate reaches somewhat higher values ($\sim 5\%$) at lower p_{T} than without pileup, but converges around 4% at higher p_{T}. The efficiency reaches a peak of about 35% around 1 TeV, and then decreases with 5 percent units decreasing over the remaining spectrum, which differs from the case without pileup where instead the efficiency remains stable at 35%. The $R = 0.4$ jets perform best under pileup, with both similar efficiency and fake rate as without. The profiles of the curves are also similar to the case without pileup.

It is possible that the larger fake rates for the two bigger jet radii, in particular $R = 1$, could be attributed to the fact that larger jets are more susceptible to pileup contamination. The HEPTopTagger searches the internal structure of the initial jet for a set of three jets that together have the characteristics of a boosted hadronic top quark decay. The larger amount of pileup in the initial, large, jet could increase the number of subjets that are possible to be constructed within it, which in turn would increase the probability for the HEPTopTagger to find a combination of subjets with the right set of kinematics to mimic a top quark decay. For example, at low p_{T}, it is possible that a QCD jet splits into a fake W which, when combined with a pileup jet, can have the appearance of a top quark decay. To determine if this indeed is the cause, further studies have to be made. Such studies, however, fall outside the scope of this thesis.

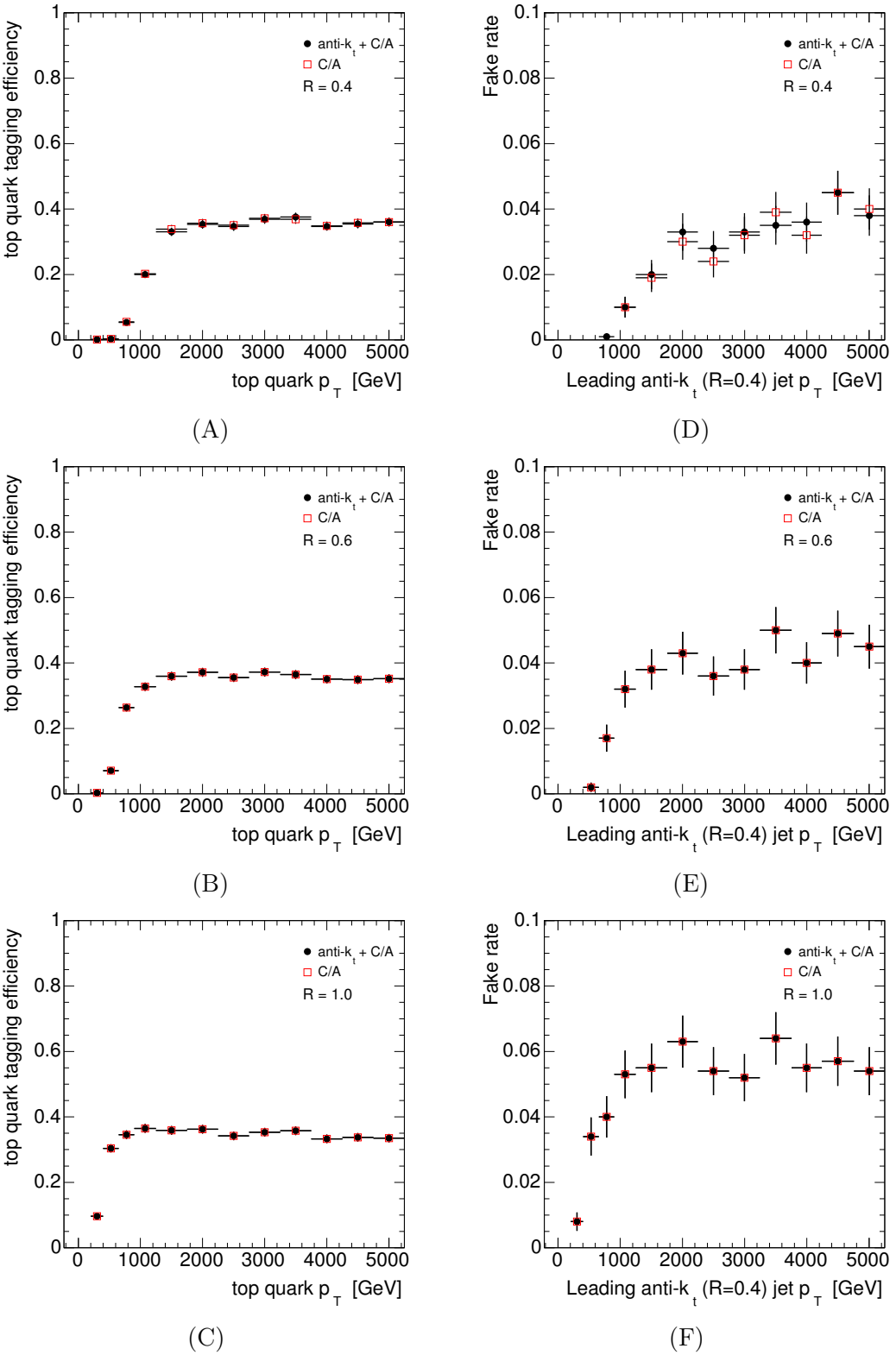

FIGURE 5.1: No detector effects. **Left:** Efficiencies for $R = 0.4, 0.6$, and 1.0 jets (A,B and C). **Right:** Fake rates for $R = 0.4, 0.6$, and 1.0 jets (D, E and F).

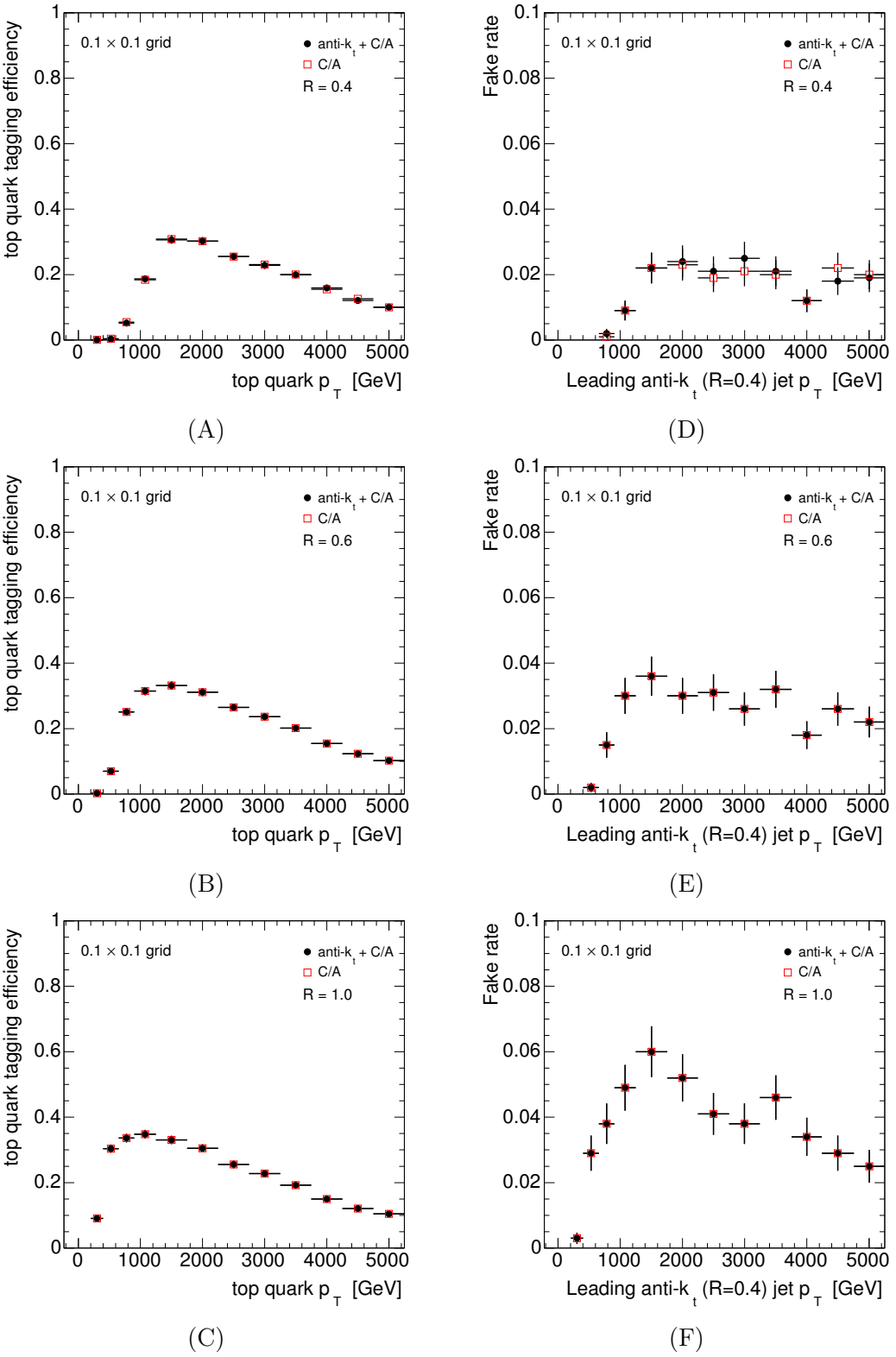

FIGURE 5.2: Simulation of detector with grid size $\Delta\eta \times \Delta\phi = 0.1 \times 0.1$. **Left:** Efficiencies for $R = 0.4, 0.6$, and 1.0 jets (A, B, and C). **Right:** Fake rates for $R = 0.4, 0.6$, and 1.0 jets (C, D, and F)

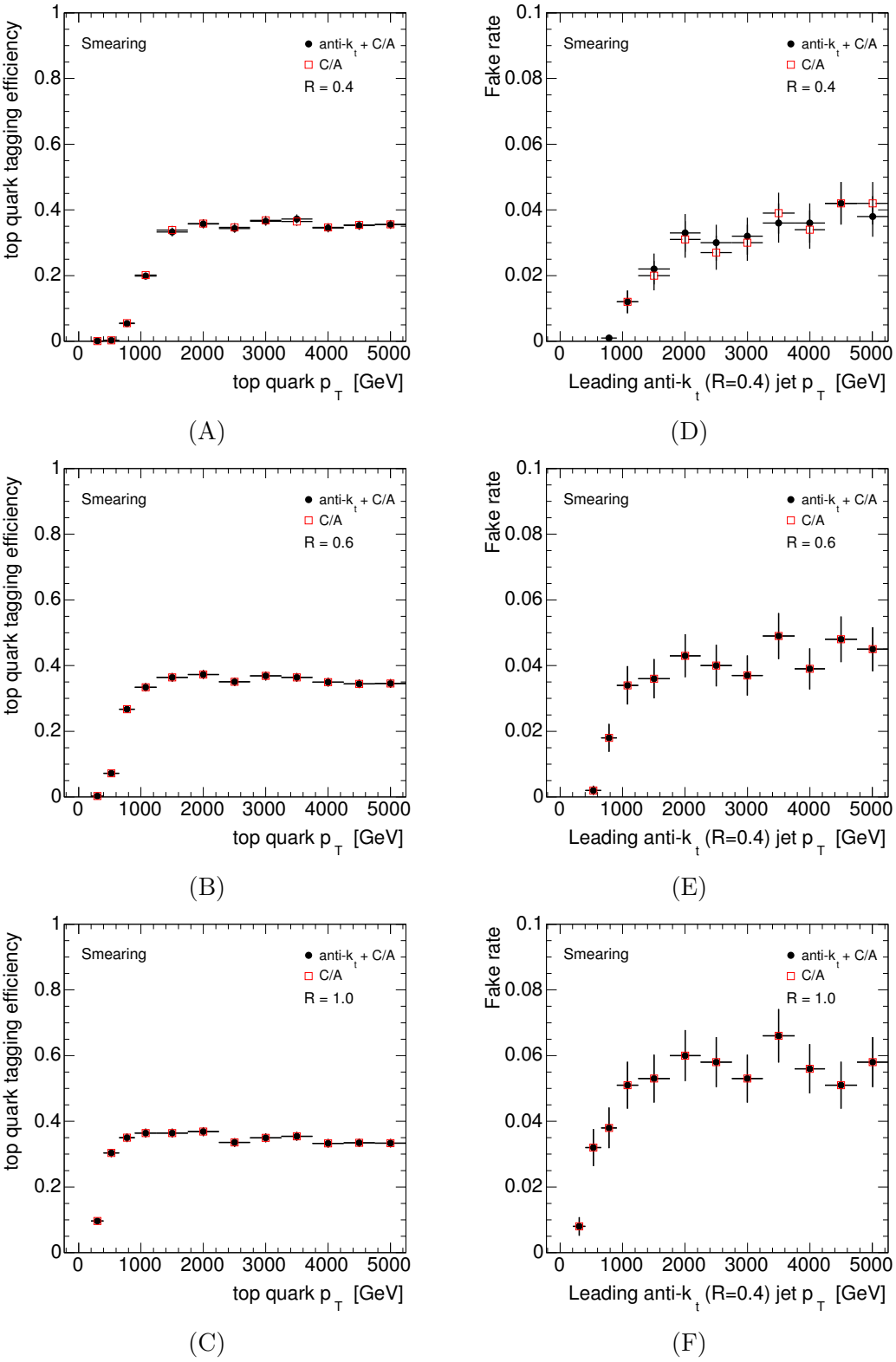

FIGURE 5.3: Simulation of detector with energy smearing. **Left:** Efficiencies for $R = 0.4, 0.6$, and 1.0 jets (top, middle, and bottom). **Right:** Fake rates for $R = 0.4, 0.6$, and 1.0 jets (top, middle, and bottom).

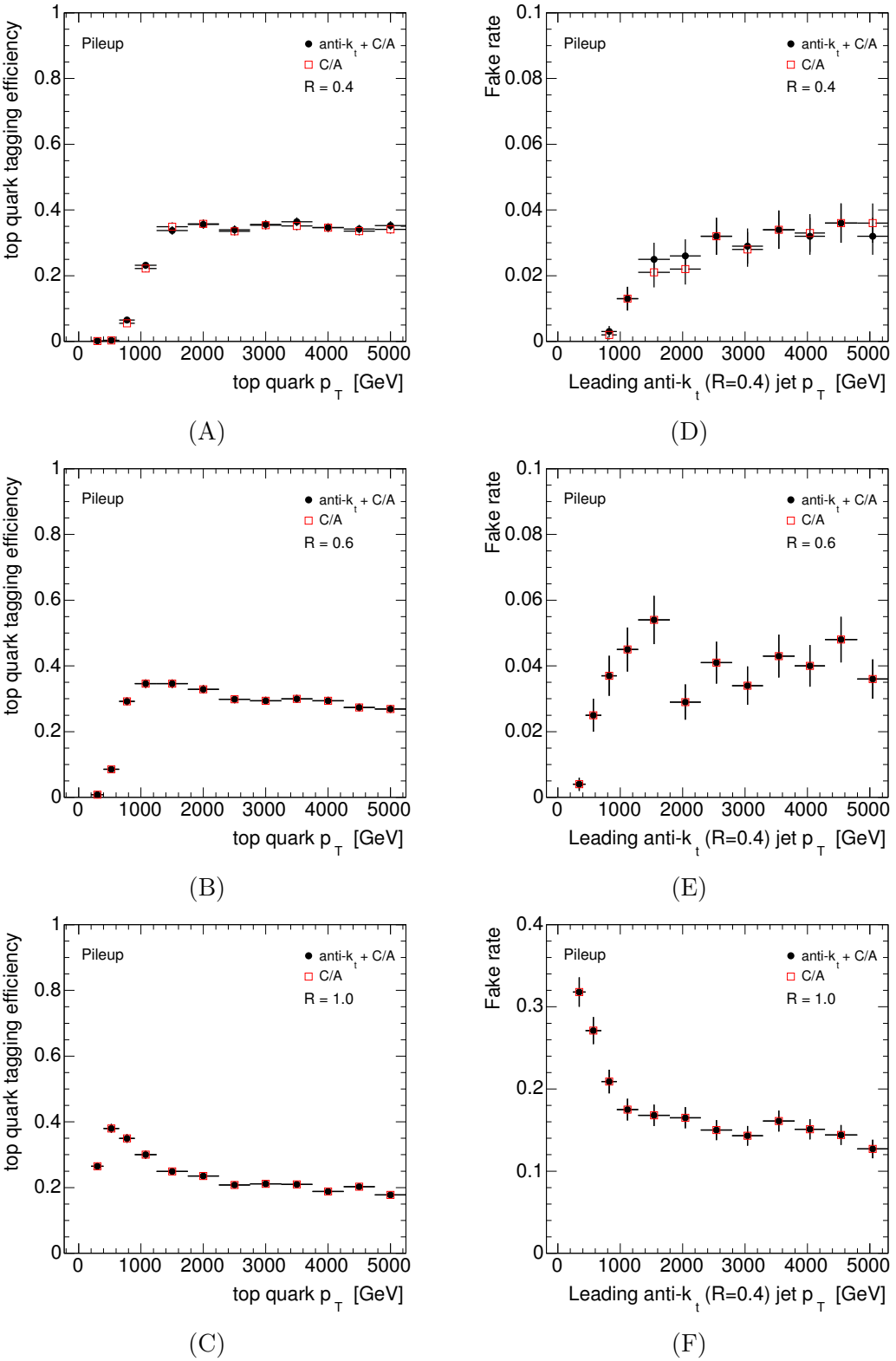

FIGURE 5.4: Simulation of pileup. **Left:** Efficiencies for $R = 0.4, 0.6$, and 1.0 jets (A, B, and C **Right:** Fake rates for $R = 0.4, 0.6$, and 1.0 jets (A, B, and C).

5.5 Conclusion

In this chapter two different procedures for the HEPTopTagger has been tested and compared: HEPTopTagger applied on jets first clustered with the anti-k_t algorithm and then reclustered with the C/A algorithm, and the standard procedure of HEPTopTagger applied on jets only clustered with the C/A algorithm. Three special cases with simulated detector effects are considered: effects from having a calorimeter with finite spatial resolution (grid), effects from limitations in energy resolution (smearing) and the effect of pileup.

It has been demonstrated that the two methods result in practically identical performance when applied on events consisting purely of $t\bar{t}$ (for testing efficiency), and on QCD events excluding $t\bar{t}$ production (for testing the fake rate), over the entire p_{T} spectrum 300 GeV to 5 TeV. This shows that the HEPTopTagger, applied on jets first clustered with the anti-k_t algorithm, can be used successfully. Generally, the relatively low efficiency of the HEPTopTagger ($\sim 35\,\%$) is compensated by its high rejection capability (with a fake rate of $\sim 4\,\%$). This makes the HEPTopTagger the top tagger of choice in ATLAS for analyses which suffer from large QCD backgrounds [38].

Three different values on the radius parameter, R, has been tested: $R = 0.4, 0.6$ and 1.0. From the tests with included detector effects, it is seen that using a radius parameter of 0.4 yields the best performance in nearly all cases; especially with pileup and grid effects. The effect of smearing is practically none for any of the parameter values.

Finally, it has been shown that the HEPTopTagger can be successfully used on highly boosted tops, even when the detector has a finite resolution comparable to, or larger, than the estimated separation between the decay products of a hadronic top decay.

Chapter 6

Analysis: Kaluza-Klein gluons

In this chapter the new HEPTopTagger routine outlined in the previous chapter is applied on simulated samples of Kaluza-Klein (KK) gluons (g_{KK}) decaying into $t\bar{t}$ pairs. This analysis only serves as a demonstration of the top tagging routine's capacity to distinguish a potential g_{KK} signal from the enormous QCD background at the LHC.

6.1 Event generation

All events (background and signal) are generated with PYTHIA8. The events are divided into three groups which are generated separately: QCD background, SM $t\bar{t}$ background, and signal (g_{KK}). The QCD background consists of hard QCD interactions, excluding those involving top quarks. The SM $t\bar{t}$ background purely consists of $t\bar{t}$ events that are produced through SM processes in the hard interaction. 100 000 QCD events and 50 000 $t\bar{t}$ events are produced, giving good background statistics. Finally, the signal consists of Kaluza-Klein gluon production exclusively decaying into $t\bar{t}$ in the context of the bulk Randall-Sundrum model. 27 260 signal events are produced, corresponding to an integrated luminosity of approximately 200 fb^{-1}. For this analysis, a KK gluon mass $M_{g_{\mathrm{KK}}} = 3$ TeV is chosen. These choices follow the scenario studied in [10]. Since the $g_{\mathrm{KK}} \to t\bar{t}$ branching ratio is 92.5% (with 5.5% to $b\bar{b}$, and the rest to light quark jets), it is reasonable to only consider the decay into $t\bar{t}$.

Both the QCD and $t\bar{t}$ backgrounds are generated over a large p_{T} range. Since many cross sections decrease rapidly with increasing transverse momentum, it is not possible to do the simulation over the whole p_{T} spectrum at once. The decreasing cross sections mean that fewer events are generated at high p_{T}, which in turn increases the statistical error. What is done instead is to divide the $\hat{p}_{\mathrm{T}}$ range into smaller subranges, with equally many

events in each subrange. The subranges are ordered such that they cover the complete $\hat{p}_{\mathrm{T}}$ spectrum without overlapping. Of course, such an approach leads to an unnatural p_{T} distribution, which is flat over the entire p_{T} interval. To achieve a natural (falling) distribution, each subrange is weighted with the integrated luminosity corresponding to that subrange. This leads to events in the tail of the lower p_{T} intervals overlapping with later intervals; these events have large weight but also large uncertainty, and introduce a small number of large fluctuations in the spectrum.

6.2 Method

The Randall-Sundrum model predicts an excess of $t\bar{t}$ events over the SM background around the mass, $M_{g_{\mathrm{KK}}}$, of the KK gluon resonance. Since the KK gluon decays primarily (in this study, exclusively) into $t\bar{t}$ pairs, the invariant mass of the combined four-vectors of the two jets, the *dijet* invariant mass m_{jj}, originating from the $t\bar{t}$ pair should serve as a good observable. The problem, as we have seen from before, is to remove the huge background without also loosing the signal. Hence the need for a top tagger.

The top tagging procedure outlined in the previous chapter is applied on the QCD events, SM $t\bar{t}$ events and signal events separately. The events are required to have at least two jets with $p_{\mathrm{T}} > 200$ GeV. The dijet invariant mass is then investigated for three cases:

1. All leading two jets,
2. When at least one jet is tagged as a top quark,
3. When exactly two jets are tagged as top quarks.

6.3 Background determination

The QCD and SM $t\bar{t}$ events are used for the background determination. The modified HEPTopTagger procedure is applied on the two types of events separately, and the resulting dijet mass distributions corresponding to each of the three cases are added together. The background shape is determined by a fit to the simulated background using the monotonically decreasing four-parameter function:

$$f(x) = p_1(1-x)^{p_2}x^{p_3+p_4\ln x}, \tag{6.1}$$

where $x = m_{jj}/\sqrt{s}$, motivated by its use in [39].

To get rid of possible large statistical fluctuations in the generated m_{jj} spectrum, a new background to the generated spectrum is made using a Poisson distribution around the fit. For simplicity, the bin-center values of the original background histogram are taken as the expected values from which the Poisson distributed random numbers are generated.

Figs. 6.1, Fig. 6.2 and 6.3 show the dijet mass background together with the fit in the cases of having two leading jets, one or more tagged jet and two tagged jets respectively.

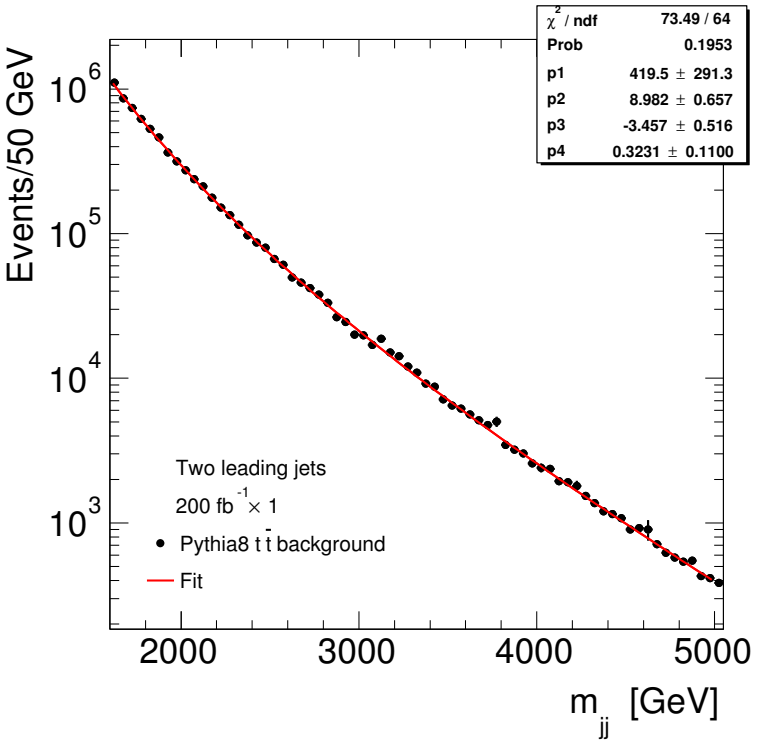

FIGURE 6.1: Full background (QCD and $t\bar{t}$) fitted with a function in the case of two leading jets.

6.4 Results

The results are divided into the three parts outlined in 6.2. Two types of figures are presented, showing 1) the superposition of the the signal and the fitted background, and 2) the probability (p-value, p_0) of getting the observed number of events, or more, given the null hypothesis that only SM processes (represented by the background) are responsible for the production of these events. The p-values are shown for integrated luminosities ranging from 5 fb^{-1} to 150 fb^{-1} .

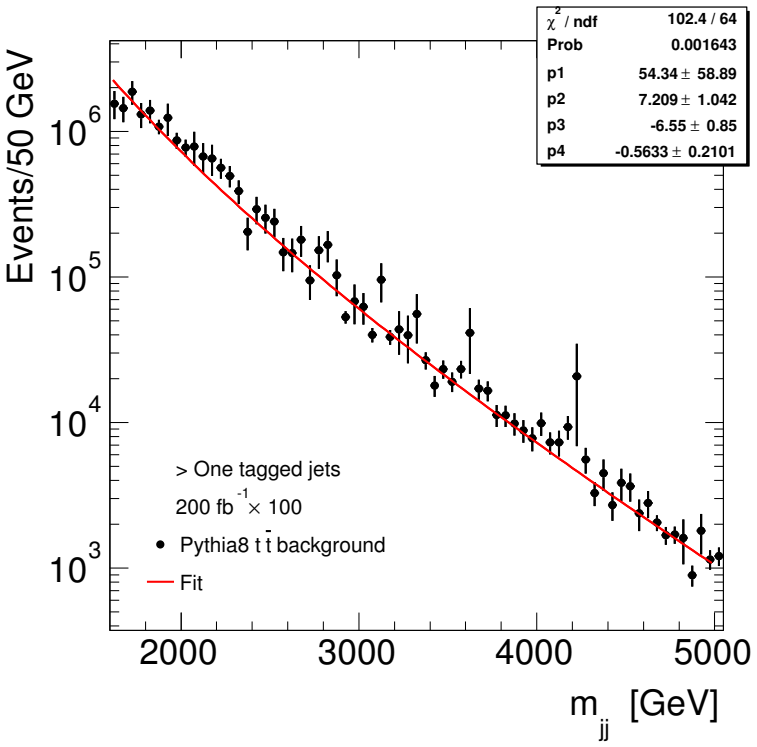

FIGURE 6.2: Full background (QCD and $t\bar{t}$) fitted with a function in the case of one tagged jet or more.

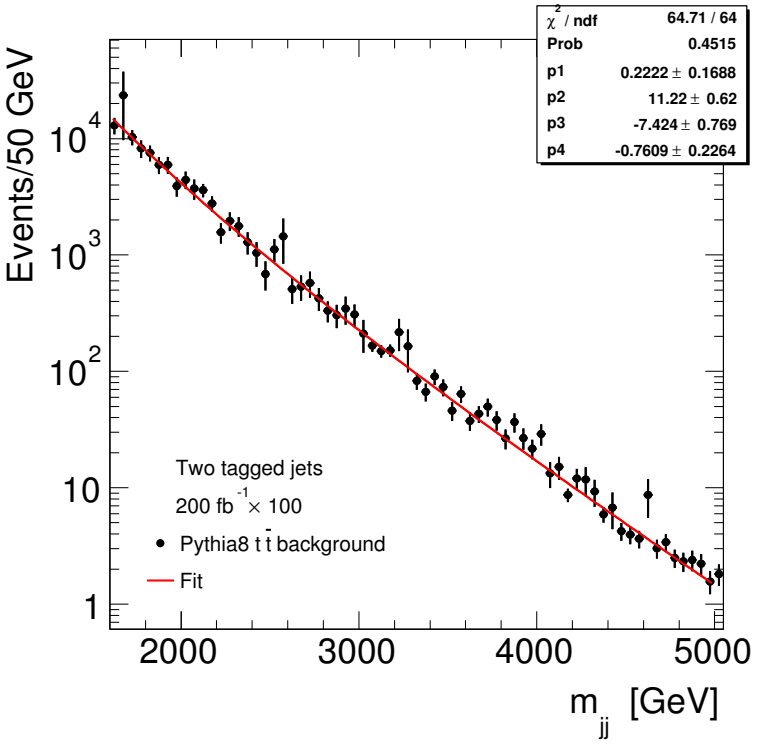

FIGURE 6.3: $t\bar{t}$ background fitted with a function in the case of two tagged jets.

6.4.1 Two leading jets

Fig 6.4 shows what the superposition of the signal and the smoothened background looks like when we try to identify top quarks using only the two hardest $R = 0.6$ jets in every event. No attempt on reducing the QCD background is made. Visual inspection of the m_{jj} spectrum in Fig. 6.4 reveals no resonance , even for the largest integrated luminosity $L = 200$ fb^{-1} . However, despite the appearance of Fig. 6.4, the p-value distribution (Fig. 6.5) show a strong significance ($> 6\sigma$) for a signal "already" at $L = 150$ fb^{-1} . It should be noted that the significance level obtained here is from a controlled environment where the background (which only contains QCD events) is known exactly. However, unless extreme care is taken in determining the background in a real experiment, it is likely that the background estimation, unknowingly, contains the signal as well. This would result in a lower significance than the one observed here.

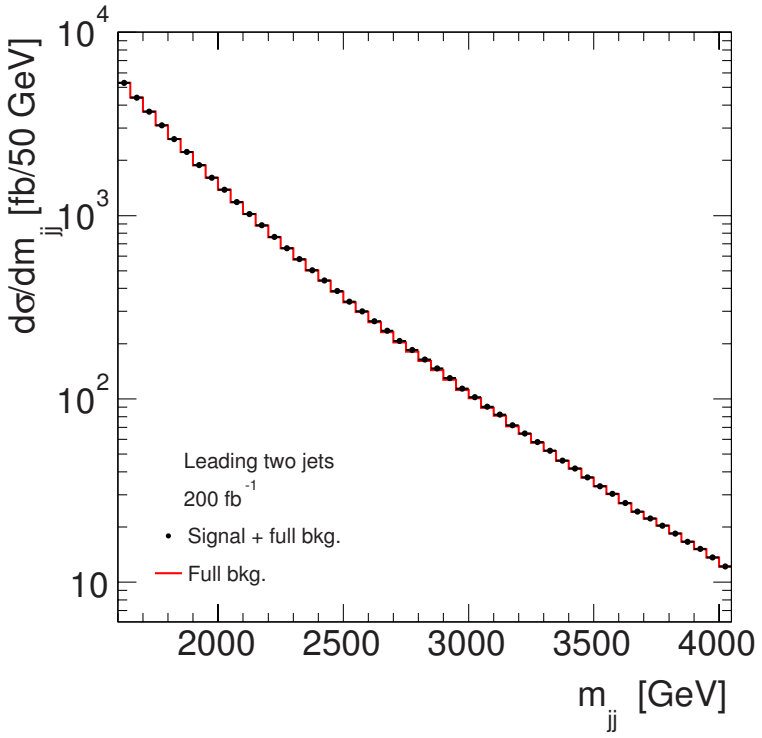

FIGURE 6.4: Dijet mass distribution for the two leading jets in each event. A smoothed full background (QCD and $t\bar{t}$) is shown together with the mass distribution of a KK gluon signal.

6.4.2 One tagged jet or more

Fig. 6.6 shows the superposition of the signal and the smoothened background when we require that *at least* one jet is tagged. A resonance around 2.9 TeV can be seen and the significance of this is established by the p-values in Fig. 6.7. Already at 50 fb^{-1} the

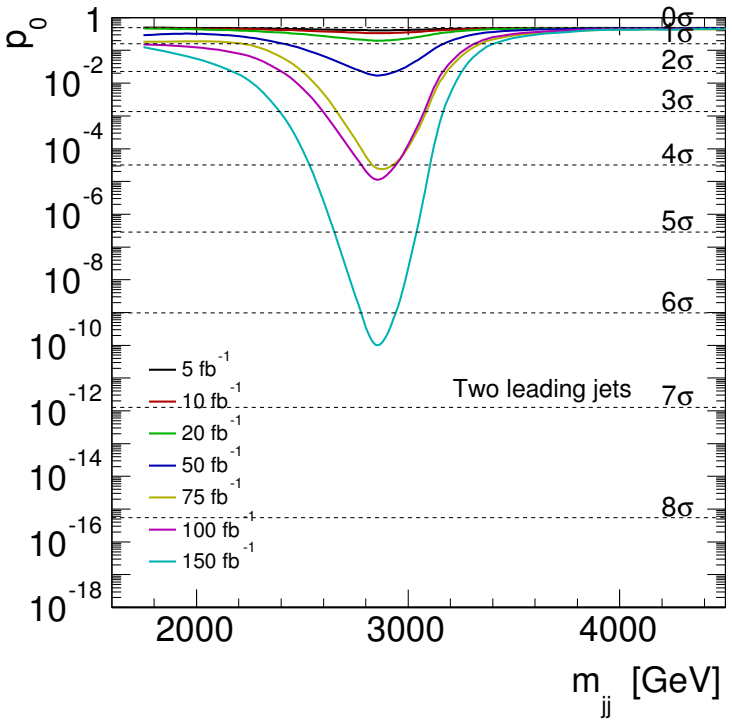

FIGURE 6.5: p-value calculation in the case of two leading jets. p_0 is the probability of obtaining the observed number of events given that the null hypothesis – that only SM processes are responsible for the production of these events – is true.

significance is $> 5\sigma$, while for 75 fb^{-1} it is past 8σ. These significances are more reliable than those obtained in section 6.4.1 since the resonance can actually be seen in the m_{jj} spectrum, which decreases the risk of bias in the background estimation.

Two tagged jets

Fig. 6.8 shows the superposition of the signal and the smoothed background when we require that exactly two jets are tagged. A very large excess of events can be seen around 2.9 TeV, amounting to one order of magnitude more than the background. However, Fig. 6.8 illustrates an important point, namely that the rejection of the background is so efficient when two tags are required that very few events are left afterwards. Thus, there is for this study little meaning in doing a p-value analysis in this case, and instead, the resonance in the m_{jj} spectrum can be visually established to be of very high significance. Naturally, a discovery like this would be extremely important, and a significant amount of analysis would be needed to verify it.

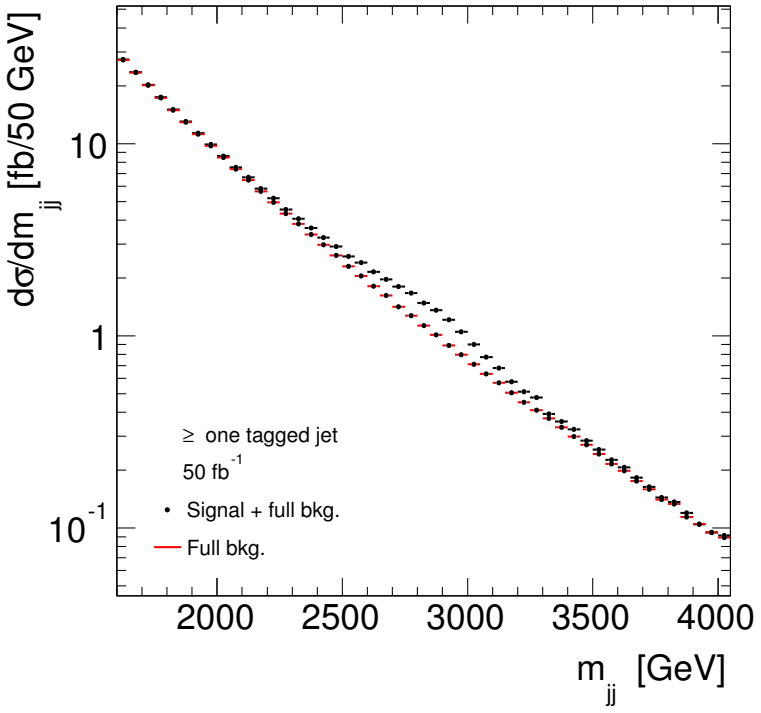

FIGURE 6.6: Dijet mass distribution in the case of one tagged jet or more in each event. A smoothed full background (QCD and $t\bar{t}$) is shown together with the mass distribution of a KK gluon signal.

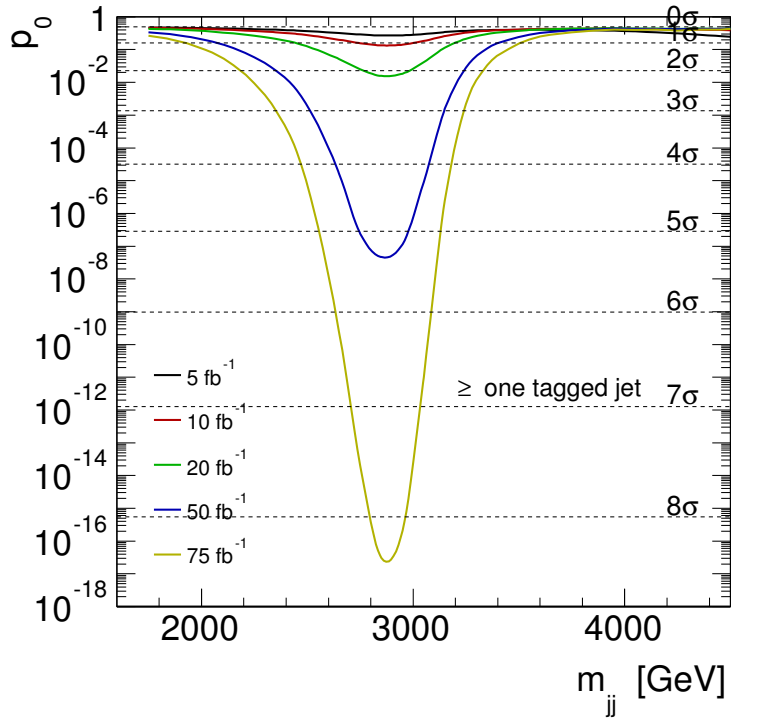

FIGURE 6.7: p-value calculation in the case of one tagged tagged jet or more. p_0 is the probability of obtaining the observed number of events given that the null hypothesis – that only SM processes are responsible for the production of these events – is true.

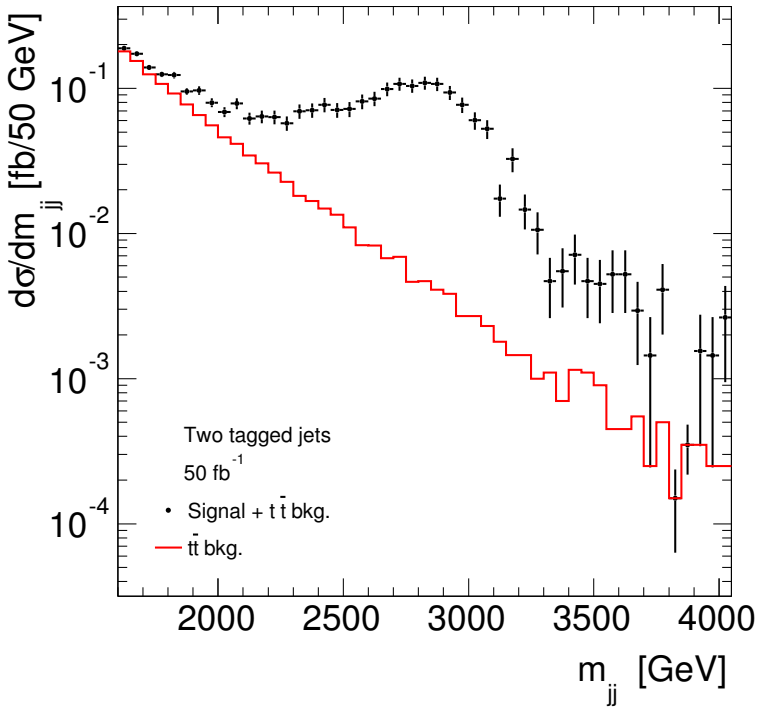

FIGURE 6.8: Dijet mass distribution in the case of two tagged jets in each event. A smoothed background ($t\bar{t}$ only) is shown together with the mass distribution of a KK gluon signal.

6.5 Conclusion

In this chapter, the HEPTopTagger algorithm was applied on jets initially clustered with the anti-k_t algorithm, with the aim of identifying boosted top quarks resulting from the decay of Kaluza-Klein gluons with mass $M_{g_{\mathrm{KK}}} = 3$ TeV in $\sqrt{s} = 14$ TeV collisions at the LHC. The analysis uses the dijet mass of top quarks as an observable since it is predicted that KK gluon decay would result in an excess of $t\bar{t}$ events with a dijet invariant mass localized around the mass of the KK gluon[10]. The effect of a detector with spatial resolution $\eta \times \phi = 0.1 \times 0.1$ has been included in the study, since it was shown in Chapter 5 to have the largest effect on the tagging performance, thus making the analysis more realistic.

It is demonstrated that a $t\bar{t}$ signal resulting from KK gluon decay can not be observed visually in the dijet mass spectrum up to 200 fb^{-1} of integrated luminosity when no effort of rejecting the background is made. It is shown, though, that significances of $> 6\sigma$ can be obtained, with the caveat that they are likely to be diminished in a real experiment in which the background estimation very well could include the signal as well. Thus, it is not likely that a discovery of a resonance could be made in this case even for very large integrated luminosities.

However, when the top tagging procedure investigated in this thesis is applied, a clear signal can be seen both when it is required that at least one top quark is tagged and when two tags are required. The two tagged case has a very clear visual significance, but suffers from the fact that because of the extremely efficient rejection, a very large integrated luminosity is needed to even tag one $t\bar{t}$ pair.

The case with at least one tagged, on the other hand, has a much smaller (while still noticeable) visual significance of the resonance, but has the advantage of including more events. This allows us to make a p-value estimation to determine the significance, which is shown to be $> 5\sigma$ at 50 fb^{-1} .

In conclusion, both cases show much potential, and it is up to discussion whether it is better to choose the procedure with one or more tagged tops over the one where two tagged tops are required. Surely, one will try both, but maybe one tag is enough.

Bibliography

[1] The ATLAS Collaboration. "Observation of a new particle in the search for the Standard Model Higgs boson with the {ATLAS} detector at the {LHC}". In: *Physics Letters B* 716.1 (2012), pp. 1 –29. DOI: http://dx.doi.org/10.1016/j.physletb.2012.08.020 (cit. on p. 7).

[2] The CMS Collaboration. "Observation of a new boson at a mass of 125 GeV with the CMS experiment at the LHC". In: *Phys.Lett.* B716 (2012), pp. 30–61. DOI: 10.1016/j.physletb.2012.08.021. arXiv: 1207.7235 [hep-ex] (cit. on p. 7).

[3] Lisa Randall and Raman Sundrum. "A Large mass hierarchy from a small extra dimension". In: *Phys.Rev.Lett.* 83 (1999), pp. 3370–3373. DOI: 10.1103/PhysRevLett.83.3370. arXiv: hep-ph/9905221 [hep-ph] (cit. on pp. 8, 9).

[4] Alex Pomarol. "Gauge bosons in a five-dimensional theory with localized gravity". In: *Phys.Lett.* B486 (2000), pp. 153–157. DOI: 10.1016/S0370-2693(00)00737-1. arXiv: hep-ph/9911294 [hep-ph] (cit. on p. 8).

[5] H. Davoudiasl, J.L. Hewett, and T.G. Rizzo. "Bulk gauge fields in the Randall-Sundrum model". In: *Phys.Lett.* B473 (2000), pp. 43–49. DOI: 10.1016/S0370-2693(99)01430-6. arXiv: hep-ph/9911262 [hep-ph] (cit. on pp. 8, 10).

[6] O. Klein. "Quantum Theory and Five-Dimensional Theory of Relativity. (In German and English)". In: *Z.Phys.* 37 (1926), pp. 895–906. DOI: 10.1007/BF01397481 (cit. on p. 8).

[7] Nima Arkani–Hamed, Savas Dimopoulos, and Gia Dvali. "The hierarchy problem and new dimensions at a millimeter". In: *Physics Letters B* 429.3–4 (1998), pp. 263 –272. DOI: http://dx.doi.org/10.1016/S0370-2693(98)00466-3 (cit. on p. 9).

[8] Thomas Appelquist, Hsin-Chia Cheng, and Bogdan A. Dobrescu. "Bounds on universal extra dimensions". In: *Phys. Rev. D* 64 (3 2001), p. 035002. DOI: 10.1103/PhysRevD.64.035002 (cit. on p. 9).

[9] J. Calvén. "Warped Extra Dimensions in the Randall-Sundrum Model and a Simple Implementation in Pythia 8". Bachelor's thesis, available at http://www.lunduniversity.lu.se/lup/publication/2302835. 2012 (cit. on p. 10).

[10] Ben Lillie, Lisa Randall, and Lian-Tao Wang. "The Bulk RS KK-gluon at the LHC". In: *J. High Energy Phys.* 2007.9 (Sept. 1, 2007), p. 074. DOI: 10.1088/1126-6708/2007/09/074 (cit. on pp. 11, 24, 41, 49).

[11] Brüning et al. *LHC Design Report*. Geneva: CERN, 2004 (cit. on p. 12).

[12] *LEP design report*. Copies shelved as reports in LEP, PS and SPS libraries. Geneva: CERN, 1984 (cit. on p. 12).

[13] The ALICE Collaboration. "The ALICE experiment at the CERN LHC". In: *Journal of Instrumentation* 3.08 (2008), S08002 (cit. on p. 12).

[14] The ATLAS Collaboration. "The ATLAS Experiment at the CERN Large Hadron Collider". In: *Journal of Instrumentation* 3.08 (2008), S08003 (cit. on pp. 12, 15).

[15] The CMS Collaboration. "The CMS experiment at the CERN LHC". In: *Journal of Instrumentation* 3.08 (2008), S08004 (cit. on p. 12).

[16] The LHCb Collaboration. "The LHCb Detector at the LHC". In: *Journal of Instrumentation* 3.08 (2008), S08005 (cit. on p. 12).

[17] The ATLAS Collaboration. "The four main LHC experiments". http://cds.cern.ch/record/40525, last viewed on September 15 2014. (cit. on p. 13).

[18] CERN. "The CERN accelerator complex". https://cds.cern.ch/record/1621894, last viewed on August 25 2014. (cit. on p. 14).

[19] The ATLAS Collaboration. "Luminosity, public results". https://twiki.cern.ch/twiki/bin/view/AtlasPublic/LuminosityPublicResults, last viewed on August 25 2014. (cit. on p. 15).

[20] The ATLAS Collaboration. "Computer generated image of the whole ATLAS detector". http://cds.cern.ch/record/1095924, last viewed on September 15 2014. (cit. on p. 16).

[21] Gavin P. Salam. "Towards Jetography". In: (June 10, 2009) (cit. on pp. 18, 21).

[22] Matteo Cacciari, Gavin P. Salam, and Gregory Soyez. "The Anti-k(t) jet clustering algorithm". In: 0804 (2008), p. 063. DOI: 10.1088/1126-6708/2008/04/063 (cit. on pp. 19, 21).

[23] ATLAS Collaboration. *Jet energy measurement with the ATLAS detector in proton-proton collisions at sqrt(s) = 7 TeV*. arXiv e-print 1112.6426. Eur. Phys. J. C, 73 3 (2013) 2304. Dec. 29, 2011 (cit. on p. 19).

[24] Davison E. Soper and Stephen D. Ellis. "Successive combination jet algorithm for hadron collisions". In: D48 (1993), pp. 3160–3166. DOI: 10.1103/PhysRevD.48.3160 (cit. on p. 21).

[25] M. Wobisch and T. Wengler. "Hadronization corrections to jet cross-sections in deep inelastic scattering". In: (1998) (cit. on p. 21).

[26] Stephen D. Ellis, Christopher K. Vermilion, and Jonathan R. Walsh. "Recombination algorithms and jet substructure: Pruning as a tool for heavy particle searches". In: *Physical Review D* 81.9 (May 2010), p. 094023. DOI: 10.1103/PhysRevD.81.094023 (cit. on p. 23).

[27] David Krohn, Jesse Thaler, and Lian-Tao Wang. "Jet trimming". en. In: *Journal of High Energy Physics* 2010.2 (Feb. 2010), pp. 1–21. DOI: 10.1007/JHEP02(2010)084 (cit. on p. 23).

[28] Jonathan M. Butterworth et al. "Jet substructure as a new Higgs search channel at the LHC". In: 100 (2008), p. 242001. DOI: 10.1103/PhysRevLett.100.242001 (cit. on p. 23).

[29] David E. Kaplan et al. "Top Tagging: A Method for Identifying Boosted Hadronically Decaying Top Quarks". In: *Phys. Rev. Lett.* 101.14 (Oct. 2, 2008), p. 142001. DOI: 10.1103/PhysRevLett.101.142001 (cit. on p. 23).

[30] J. Beringer et al. "Review of Particle Physics". In: *Phys. Rev. D* 86 (2012), p. 010001 (cit. on p. 24).

[31] Frank-Peter Schilling. "Top Quark Physics at the LHC: A Review of the First Two Years". In: *Int.J.Mod.Phys.* A27 (2012), p. 1230016. DOI: 10.1142/S0217751X12300165. arXiv: 1206.4484 [hep-ex] (cit. on p. 24).

[32] S. Fleischmann. "Boosted top quark techniques and searches for $t\bar{t}$ resonances at the LHC". In: *J.Phys.Conf.Ser.* 452.1 (2013), p. 012034. DOI: 10.1088/1742-6596/452/1/012034 (cit. on p. 26).

[33] Tilman Plehn et al. *Stop Reconstruction with Tagged Tops*. arXiv e-print 1006.2833. JHEP 1010:078,2010. June 14, 2010 (cit. on pp. 26, 27).

[34] The ATLAS Collaboration. *Performance of large-R jets and jet substructure reconstruction with the ATLAS detector*. CERN Document Server. July 4, 2012. URL: http://cds.cern.ch/record/1459530 (visited on 02/08/2014) (cit. on pp. 26–28, 33).

[35] H.L. Lai et al. "Global QCD analysis of parton structure of the nucleon: CTEQ5 parton distributions". In: *Eur.Phys.J.* C12 (2000), pp. 375–392. DOI: 10.1007/s100529900196. arXiv: hep-ph/9903282 [hep-ph] (cit. on p. 30).

[36] Francesca Cavallari. "Performance of calorimeters at the LHC". In: *Journal of Physics: Conference Series* 293.1 (2011), p. 012001 (cit. on p. 31).

[37] The ATLAS Collaboration. *Pile-up subtraction and suppression for jets in ATLAS*. Tech. rep. ATLAS-CONF-2013-083. Geneva: CERN, 2013 (cit. on p. 32).

[38] The ATLAS Collaboration. *Performance of boosted top quark identification in 2012 ATLAS data*. Tech. rep. ATLAS-CONF-2013-084. Geneva: CERN, 2013 (cit. on p. 40).

[39] The ATLAS Collaboration. "ATLAS search for new phenomena in dijet mass and angular distributions using pp collisions at $\sqrt{s} = 7$ TeV". In: *JHEP* 1301 (2013), p. 029. DOI: 10.1007/JHEP01(2013)029. arXiv: 1210.1718 [hep-ex] (cit. on p. 42).